Power Electronic Systems
Laboratory

© 2022 IEEE

IEEE Journal of Emerging and Selected Topics in Power Electronics, Vol. 10, No. 4, pp. 3541-3560, August 2022

Design and Experimental Analysis of 166 kW Medium-Voltage Medium-Frequency Air-Core Transformer for 1:1-DCX Applications

P. Czyz,
T. Guillod,
F. Krismer,
J. Huber,
J. W. Kolar

Personal use of this material is permitted. Permission from IEEE must be obtained for all other uses, in any current or future media, including reprinting/republishing this material for advertising or promotional purposes, creating new collective works, for resale or redistribution to servers or lists, or reuse of any copyrighted component of this work in other works

Eidgenössische Technische Hochschule Zürich
Swiss Federal Institute of Technology Zurich

This is the author's version of an article that has been published in this journal. Changes were made to this version by the publisher prior to publication.
The final version of record is available at http://dx.doi.org/10.1109/JESTPE.2021.3060506

Design and Experimental Analysis of 166 kW Medium-Voltage Medium-Frequency Air-Core Transformer for 1:1-DCX Applications

Piotr Czyz, *Student Member, IEEE*, Thomas Guillod, *Member, IEEE*, Florian Krismer, *Member, IEEE*, Jonas Huber, *Member, IEEE* and Johann W. Kolar, *Fellow, IEEE*
Power Electronic Systems Laboratory (PES), ETH Zurich, Switzerland
Corresponding Author: Piotr Czyz (czyz@lem.ee.ethz.ch)

***Abstract*—The galvanic isolation of solid-state transformers (SSTs) is typically realized with a medium-frequency (MF) magnetic-core transformer (MCT). Previous demonstrations indicate that achieving highly power dense and lightweight MCTs imposes several challenges on the design because of stringent requirements related to insulation and cooling. This work investigates the achievable efficiency of an optimized 166 kW / 7 kV air-core transformer (ACT), which is a core part of a DC Transformer (DCX), i.e., an unregulated DC-DC SST with a voltage scaling defined by the transformer turns ratio. The ACT features relatively low complexity of the construction, comparably high coupling values, and high efficiency. Modeling, optimization, and construction of the realized ACT are explained and guidelines regarding insulation, cooling, and shielding of the magnetic stray flux are discussed in detail. Furthermore, the prototype is experimentally validated to demonstrate its full functionality. In the investigated DCX, which is based on a series resonant converter (SRC) topology, the realized ACT is found to achieve a full-load efficiency of 99.5 % and an unprecedented gravimetric power density of 16.5 kW/kg. With the use of 10 kV SiC MOSFETs, the complete DCX is estimated to reach an efficiency of 99 % at 166 kW output power.**

***Index Terms*—DC transformer (DCX), air-core transformer (ACT), medium-frequency (MF), medium-voltage (MV), solid-state transformers (SSTs).**

I. Introduction

Solid-state transformers (SSTs) provide galvanic isolation between two or more ports by means of medium-frequency (MF) transformers, whereby at least one port operates at medium-voltage (MV) levels (i.e., at voltages higher than 1 kV). Typical power levels range from 50 kW to several megawatts. These characteristic properties render SSTs a key component for a wide range of emerging applications, such as future hybrid smart grid systems with AC and DC sections [1], [2], grid interfaces for renewable power sources [3], [4], hyperscale data centers [5], [6], high-power EV charging stations [7], [8], future ships [9]–[11], and future aircraft with distributed propulsion and on-board MVDC grids [12]–[14].

The SST's key component, i.e., the medium-frequency transformer (MFT), is typically realized as a magnetic-core transformer (MCT), preferably as a dry-type MCT. However, the design of the MCT is challenging, mainly because of stringent requirements related to insulation and cooling, e.g., the need for void-free potting of the windings, handling of increased thermal resistances, and higher parasitic capacitances [15]. Furthermore, the mass of the magnetic cores and of the dry-type insulation limits the achievable gravimetric power density [6], [16], [17], which is clearly a drawback for the airborne applications mentioned above, but may also complicate handling during production and assembly in general.

Air-core transformers (ACTs) represent an interesting alternative as, by definition, they lack a magnetic core and hence the windings must still be isolated from each other but not from a magnetic core. This, in turn, facilitates the use of air as insulation medium and, simultaneously, for direct cooling of the windings. Hence, ACTs feature comparably straightforward construction and can achieve high gravimetric power densities; however, a lower volumetric power density must be expected. Recent publications reveal that high-power inductively coupled wireless power transfer (WPT) systems can reach high efficiencies close to 99 % and allow for overall DC-DC converter efficiencies up to about 96 % [18], even though these systems typically employ planar coils with relatively low coupling factors. The achievable efficiency of such inductive power transfer (IPT) systems increases with the product of quality factor and coupling coefficient [19]. Since for stationary applications alternative coil geometries with potentially higher coupling factors than planar coils (at similar quality factors) can be explored, ACT designs for SST applications should be able to achieve efficiencies considerably higher than 99 %. Furthermore, by taking advantage of available SiC power semiconductors that feature a high blocking voltage capability and a low on-state resistance, the realization of an ACT-based isolated DC-DC converter with an efficiency of close to 99 %, which is a typical target efficiency for SSTs, seems to be feasible, even considering that relatively high operating frequencies are necessary due to the low magnetizing inductance of an ACT (e.g., 85 kHz is a typical value for high-power IPT systems [18], [20]).

This paper analyzes an ACT that is the key component of a series resonant converter (SRC) operated at the resonance frequency, which therefore acts as a DC transformer (DCX) [6], [22]–[24], i.e., tightly couples the DC input and output voltages without the need for closed-loop control. **Tab. I** lists the system's key specifications.

We consider a unity ratio of primary-side to secondary-

Copyright (c) 2021 IEEE. Personal use is permitted. For any other purposes, permission must be obtained from the IEEE by emailing pubs-permissions@ieee.org.

This is the author's version of an article that has been published in this journal. Changes were made to this version by the publisher prior to publication.
The final version of record is available at http://dx.doi.org/10.1109/JESTPE.2021.3060506

TABLE I. Specifications of the ACT-based 1:1-DCX.

P_N	166 kW	output power
V_{DC}	7 kV(±3.5 kV)	input and output DC voltage
V_i	10 kV DC	isolation voltage between primary and secondary side

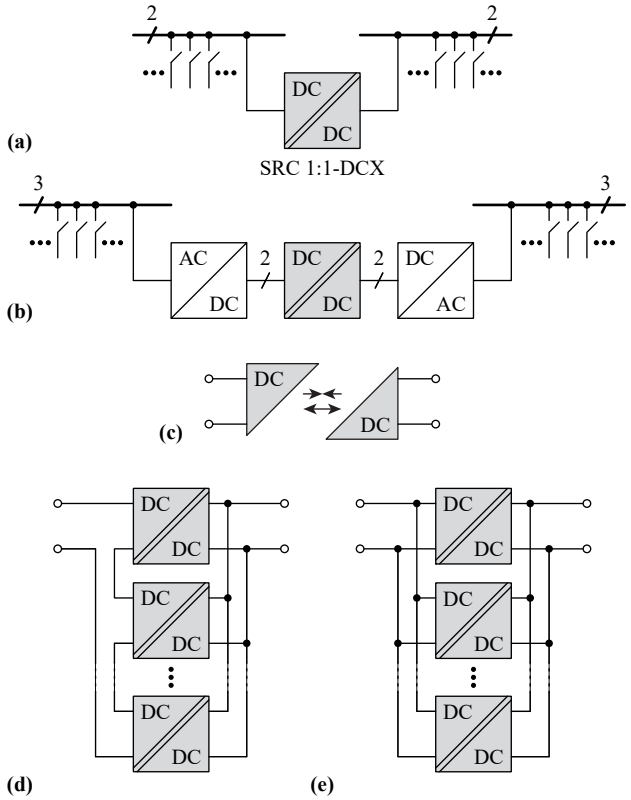

Fig. 1. 1:1-DCX applications and options for scaling voltage and power ratings. **(a)** 1:1-DCX as a power electronic link between two MVDC buses, acting as a flexible bus-tie switch. **(b)** Coupling of two AC grids [21], where the 1:1-DCX provides isolation and dedicated AC-DC converters control the power flows. **(c)** An air-core transformer facilitates the realization of contactless and spark-free plugs, e.g., for subsea applications. Combinations of several 1:1-DCX in either **(d)** input-series, output-parallel (ISOP) or **(e)** input-parallel, output-parallel (IPOP) configuration facilitate a scaling to higher overall voltage or power ratings.

side DC port voltages (1:1-DCX), which is suitable for several applications: in DC bus-tie applications [11] (see **Fig. 1(a)**), the galvanic isolation of the 1:1-DCX enables a more flexible grounding of subsystems than conventional switches or connectors do. In open-loop operation it ensures equal bus voltages and free bidirectional exchange of power. Furthermore, the 1:1-DCX can provide power flow control or output current limitation, e. g., by employing the quantum operating mode introduced in [25]. To facilitate the coupling of two AC grids [21], the 1:1-DCX can be complemented by AC-DC and DC-AC converters, which then take over the power flow control, see **Fig. 1(b)**. Furthermore, because of the absence of a magnetic core, an ACT lends itself to the realization of contactless (and hence spark-free) plugs (see **Fig. 1(c)**), which could find use in subsea applications or in other harsh or explosion-prone environments such as in mining [26]–[29]. Finally, a 1:1-DCX facilitates straightforward high-power back-to-back testing, i.e., the secondary-

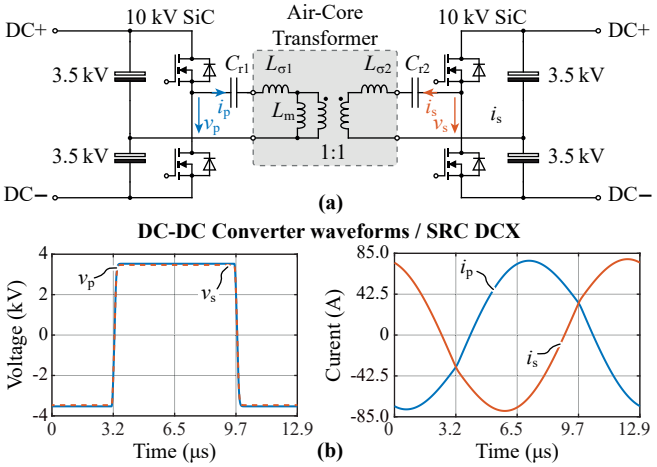

Fig. 2. (a) Converter topology of the 166 kW / 7 kV SRC 1:1-DCX. **(b)** Simulated current and voltage waveforms at rated power and with an operating frequency of $f_s = 77.4$ kHz.

side DC port can be directly connected back to the primary-side DC port. In this configuration, the system can be tested at high rated power levels with the supply only covering the comparably low losses of the system [18]. Moreover, as shown in **Fig. 1(d)** and **(e)**, several 1:1-DCX converters can be combined to scale the overall voltage or power rating, depending on the application. Note that the input-series, output-parallel (ISOP) configuration would require a higher isolation voltage rating between the transformer's primary and secondary windings. Using an input-parallel, output-parallel (IPOP) configuration of six 166 kW-1:1-DCX converters, a 1 MW system could be realized.

Fig. 2 shows the SRC topology of the 1:1-DCX converter and exemplary key waveforms. The two series resonant capacitors, C_{r1} and C_{r2}, are chosen such that they compensate the corresponding ACT stray inductances, $L_{\sigma1}$ and $L_{\sigma2}$, at the operating frequency, which thus equals the resonant frequency, i.e., $f_s = f_0 = 1/(2\pi\sqrt{C_{r1}L_{\sigma1}} = 1/(2\pi\sqrt{C_{r2}L_{\sigma2}})$. This enables a tight coupling of the two DC bus voltages without the need of closed-loop control [6]. Considering the selected DC bus voltage of 7 kV, available 10 kV SiC MOSFETs can be employed with sufficient margin regarding the blocking voltage utilization. The realization with one half-bridge and one capacitive voltage divider per bridge requires only half the number of switches compared to a full-bridge [30]. Advantageously, the SRC converter features zero-voltage switching (ZVS) over the full load range, which is supported by the magnetizing current that appears in the primary- and secondary-side half bridges [22], and well-defined voltages across the switches.

In this context, this paper first covers generic realization options and coil arrangements for ACTs in **Section II**. **Section III** then provides an in-depth discussion of the modeling and the multi-objective optimization of the 166 kW / 7 kV ACT. **Section IV** covers the actual hardware design of the optimized ACT, including details related to the isolation system and the conductive shielding that limits magnetic stray fields in the ACT's surroundings. Furthermore, we conduct a thorough experimental analysis of the full-scale ACT prototype in **Section V**. This includes small-

Copyright (c) 2021 IEEE. Personal use is permitted. For any other purposes, permission must be obtained from the IEEE by emailing pubs-permissions@ieee.org.

This is the author's version of an article that has been published in this journal. Changes were made to this version by the publisher prior to publication.
The final version of record is available at http://dx.doi.org/10.1109/JESTPE.2021.3060506

signal measurements, large-signal waveforms, calorimetric loss measurements, and measurements of magnetic flux densities in the vicinity of the ACT to assess the efficacy of the shielding. **Section VI**, finally, discusses the efficiency characteristics of the ACT and the complete 1:1-DCX. The realized ACT prototype achieves a measured efficiency of $99.5\,\%$ for output power levels between $25\,\mathrm{kW}$ and $166\,\mathrm{kW}$, and a gravimetric power density of $16.5\,\mathrm{kW/kg}$. With the use of $10\,\mathrm{kV}$ SiC MOSFETs, the complete 1:1-DCX can attain an efficiency of $99\,\%$ at rated output power.

II. Basic Air-Core Transformer Configurations

An ACT consists of at least one primary-side and one secondary-side coil, which can be arranged in various configurations. This section provides a brief survey and an initial, qualitative comparison of such realization options to identify the most suitable one for further optimization and design considerations. In addition, we introduce the two basic options (i.e., employing magnetic or conductive materials) to provide shielding against excessive magnetic stray fields.

A. Coil Arrangements

A first promising arrangement for the realization of an ACT uses planar coils as are typical for IPT/WPT systems [31], cf. **Fig. 3(a)**. Various lateral coil shapes have been employed, e.g., spiral [19], rectangular [19], [32] or double-D [18], [33], [34]. Planar coils are advantageous because they facilitate straightforward solutions for thermal management and insulation. High-power IPT systems typically achieve high efficiencies by adding magnetic cores to guide the magnetic fields (mainly on the non-mating sides of the coils), which increases the coupling and simultaneously contributes to the shielding of the magnetic stray flux [18], [31], [34]. The mass of the magnetic cores limits the achievable gravimetric power density, which is an important aspect regarding airborne applications and, more generally, handling considerations. Literature on high-power air-core IPT systems, i.e., planar coil arrangements without any magnetic material, is very scarce; however, a corresponding $40\,\mathrm{kW}$ system recently reported in [32] is characterized by a relatively low overall DC-DC efficiency of around $90\,\%$. Even though for stationary applications such arrangements of planar coils can be expected to achieve higher coupling than typical, mobility-oriented IPT/WPT systems (e.g., because a shorter air gap between the coils may be feasible) and hence higher efficiency, the absence of cores would require other means for shielding of the magnetic stray flux. Most important, however, the bounding-box geometry of planar IPT coil arrangements has essentially only two degrees of freedom as they are necessarily flat, i.e., the lateral dimensions become larger with increasing power transfer capability. The possible aspect ratios are thus constrained and may not be suitable for some of the various potential ACT applications discussed in the previous section.

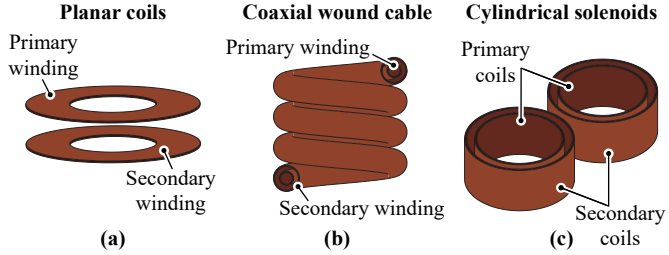

Fig. 3. Considered coil arrangements for the ACT realization: **(a)** (spiral) planar coils; **(b)** coaxially wound cable in a solenoid arrangement; **(c)** cylindrical solenoids.

Regarding MCTs with unity turns ratio and high isolation voltage requirements, windings made of a coaxial MV cable wound onto a magnetic core have been proposed [35]–[37]. Advantageously, this arrangement contains the leakage flux within the inter-winding space, i.e., between the core (primary-side winding) and the metallic shield (secondary-side winding) of the coaxial cable, which inherently provides galvanic isolation, too. The cooling of the inner winding, on the other hand, is not straightforward, and requires a comparably complex liquid- or forced-air cooling system. Furthermore, an ACT in this configuration (cf. **Fig. 3(b)**) would require long multi-turn coils [38] to achieve a sufficiently high magnetizing inductance. This complicates the manufacturing and cooling of the windings and a relatively low coupling must be expected even for a multi-turn coaxial-cable ACT; therefore we do not pursue this option further.

In [13] we proposed an ACT configuration consisting of a pair of coaxial solenoids, cf. **Fig. 3(c)**, i.e., essentially a winding configuration similar to that of a core-type MCT, but without a magnetic core (and adapted dimensions). This coil arrangement achieves relatively high coupling for the considered insulation voltages, features low-complexity construction and isolation (air), as well as simplified thermal management, as large surfaces are available for direct (forced) air cooling. Because of these favorable characteristics, we consider this coil arrangement for the subsequent optimization and design of a high-power MV MF ACT. Note that the magnetic stray flux in the proximity of the ACT must be limited, which requires some sort of shielding (see **Section II-C** below). First, however, we discuss different possibilities for interconnecting the arrangement's four coils shown in **Fig. 3(c)** to form a four-terminal (i.e., two primary-side and two secondary-side terminals) transformer.

B. Coil Interconnections

Considering the interconnections of the four coils, the straightforward approach would be to use two identical sets of two coaxially arranged coils, e.g., with the inner coils being connected in series to form the primary winding and the two outer coils connected likewise to form the secondary winding. **Fig. 4(a)** shows a 2-D finite-element method (FEM) simulation of the magnetic field for this case as well as extracted self inductances of the primary-side winding, L_p, and of the secondary-side winding, L_s, which are *asymmetric* (essentially because the diameters of both primary-side coils are larger than those of the two secondary-side coils).

Inverting the winding direction of the coils in one set achieves partial cancellation of the magnetic stray flux, as shown in **Fig. 4(b)**. However, whereas the coupling increases slightly, L_p and L_s remain similarly asymmetric as before.

Copyright (c) 2021 IEEE. Personal use is permitted. For any other purposes, permission must be obtained from the IEEE by emailing pubs-permissions@ieee.org.

This is the author's version of an article that has been published in this journal. Changes were made to this version by the publisher prior to publication.
The final version of record is available at http://dx.doi.org/10.1109/JESTPE.2021.3060506

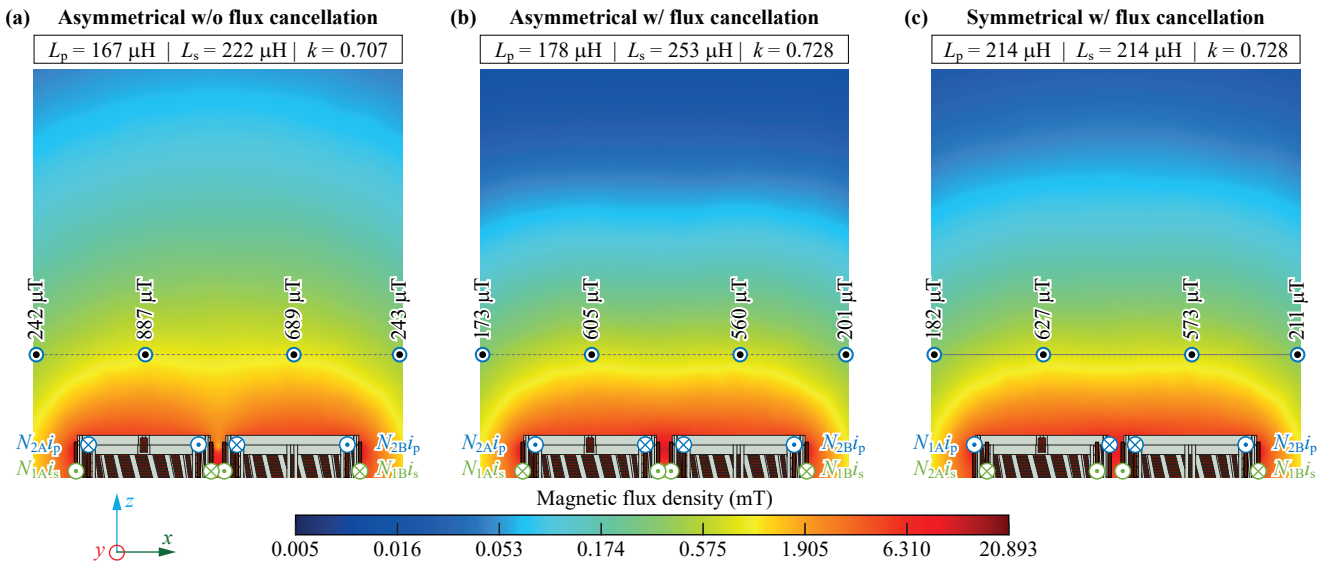

Fig. 4. FEM-simulated flux densities within the cut plane defined in **Fig. 5**: **(a)** coil interconnections with asymmetrical L_p (coils 2A with 2B) and L_s (coils 1A with 1B) without magnetic stray flux cancellation; **(b)** asymmetrical connections of the two sets of coils with partial cancellation of magnetic stray flux (note the inverted sense of winding of the coils on the left); **(c)** proposed coil interconnections with partial cancellation of magnetic stray flux and symmetrical self inductances L_p and L_s (note that the primary-side and the secondary-side winding each comprise one outer and one inner coil). In the simulations, nominal primary- and secondary-side currents, i_p and i_s respectively, are used.

Thus, **Fig. 4(c)** shows a *symmetric* interconnection of the coils, where the primary- and the secondary-side windings consist of one outer and one inner coil each, i.e., the series connection of coil 1A and coil 2B forms the primary-side winding, and the series connection of coil 1B and coil 2A forms the secondary-side winding (see **Fig. 5** for the definitions of the coil identifiers). Furthermore, the winding directions are such that again partial stray flux cancellation is achieved, i.e., the magnetic flux density averaged over the points indicated in the figure is about 25 % lower for the symmetrical case when compared to the asymmetrical interconnection without flux cancellation from **Fig. 4(a)**, however, 5 % higher than for the asymmetrical configuration with flux cancellation from **Fig. 4(b)**. Nonetheless, the benefits of symmetrical self inductances on the system level are significant: as the 1:1-DCX is then symmetric, too, it can operate with identical series resonant capacitance values on both sides of the transformer, which facilitates construction using standardized building blocks, e.g., resonant capacitor banks.

Thus, we consider two coaxially-arranged, cylindrical primary- and secondary-side windings and the symmetrical coil interconnection approach for the further analysis of the MV/MF ACT, see **Fig. 5**, which also shows the corresponding lossless linear equivalent circuit. Since the primary- and secondary-side self inductances are symmetric, i.e., $L_p \approx L_s$, so are the two leakage inductances, i.e., $L_{\sigma 1} \approx L_{\sigma 2}$.

Note that a turns ratio of $n = 2:1$ could be realized by simply connecting the two coils of the secondary winding in parallel, i.e., employing an ISOP configuration of the transformer windings. To ensure equal current sharing among the two parallel-connected secondary-side coils, they must be geometrically identical, i.e., a configuration according to **Fig. 4(b)** must be used. However, a further evaluation of such a configuration is beyond the scope of this paper.

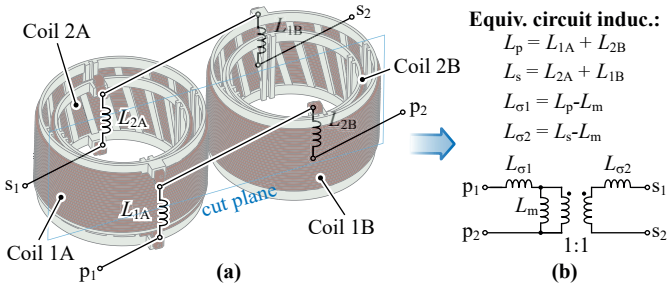

Fig. 5. **(a)** CAD rendering showing the selected coil arrangement with coil interconnections according to **Fig. 4(c)**: the series connection of L_{1A} and L_{2B} forms the primary-side self inductance, L_p, and the same applies for the secondary side. **(b)** Lossless linear equivalent circuit of the ACT. Overall, the primary- and secondary-side windings are symmetrical, thanks to the implemented interconnections between the coil sets A & B.

C. Shielding Configurations

As mentioned above, shielding must be provided to limit the values of the magnetic stray flux densities in the proximity of the ACT, whereby magnetic or conductive shielding materials can be considered. Shielding concepts that employ flux-guiding magnetic materials such as ferrite increase the weight of the system significantly [13], which is a consequence of the high density of the material and of the required material thickness to avoid saturation.

Alternatively, conductive shielding materials, e.g., copper or aluminum, can be considered [18]. The shielding effect is then achieved through a compensating field produced by eddy currents that are induced in the conductive material. As quite thin (e.g., 0.5 mm) aluminum sheet metal provides sufficiently low resistances for these eddy currents to circulate without generating excessive losses, we only

Copyright (c) 2021 IEEE. Personal use is permitted. For any other purposes, permission must be obtained from the IEEE by emailing pubs-permissions@ieee.org.

This is the author's version of an article that has been published in this journal. Changes were made to this version by the publisher prior to publication.
The final version of record is available at http://dx.doi.org/10.1109/JESTPE.2021.3060506

consider this approach to realize a lightweight and cost-effective shielding.

III. Modeling and Optimization

The selected arrangement and interconnection scheme of the coils define the general geometry of the ACT, see **Fig. 5**. However, the actual dimensions (e.g., coil diameters, width and length of the windings), the number of turns, and the operating frequency are free parameters. In the following, we introduce detailed 2-D and 3-D FEM models of the ACT that enable a multi-objective Pareto optimization. The optimal set of parameters can then be selected by taking into account the performance of the overall 1:1-DCX as well.

A. 2-D and 3-D FEM Modeling of the ACT

For a given geometry, 2-D and 3-D FEM simulations of the electromagnetic fields are used to parametrize the ACT equivalent circuit from **Fig. 5(b)**, without considering the conductive shielding. Three different levels of detail have been considered in the course of this analysis and **Fig. 6** illustrates the corresponding models. The *first model*, depicted in **Fig. 6(a)**, is based on 2-D FEM simulations of one of the two coil sets A or B. The component values needed for the equivalent model of the entire ACT, see **Fig. 5(b)**, are then determined from the individual values computed for the two coils in the considered set. The *second model* (3-D simple, **Fig. 6(b)**) uses 3-D FEM and approximates each coil with a solid hollow cylinder. Finally, the *third model* (3-D detailed, **Fig. 6(c)**) considers each turn of the coils individually with a circular cross section and thus achieves highest accuracy. The FEM simulations utilize all available symmetry planes to reduce the computational effort, however, in case of 3-D FEM, only quarter symmetries exist, due to the coil sets' interconnections described above and shown in **Fig. 5(c)**.

Tab. II shows a comparison of the accuracies (with respect to the 3-D FEM detailed simulation) and the required computing demands of the presented methods. For the benchmarking, we use a mid-range laptop (Intel Core i7-7600U with 20 GB RAM). The approach with 2-D FEM is best suited for the optimization runs, since it features lowest computational demands and sufficient accuracy (the deviations are in the range of 5 %, since the approach slightly underestimates the coupling factor due to the independent consideration of the two coil sets). Moreover, the simple 3-D FEM simulation provides a very good matching (deviation below 3 %) and is thus used to verify the finally selected design of the ACT.

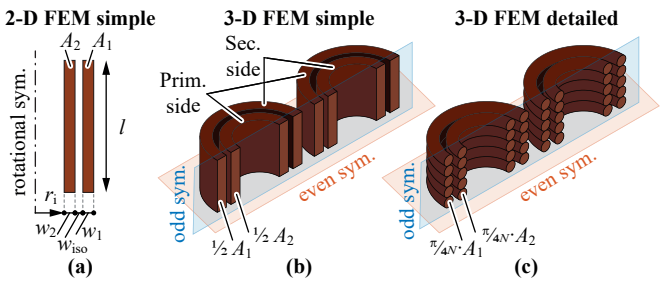

Fig. 6. (a) 2-D FEM model for one set of the coils and a simplified winding geometry (rectangular winding cross section). **(b)** 3-D FEM model with a simplified winding geometry and two sets of coils, **(c)** 3-D FEM model with a detailed winding geometry (individual turns with circular cross sections). The shown symmetry planes reduce the complexities of the models.

TABLE II. Comparison of selected results obtained with different modeling methods: 2-D FEM, 3-D FEM simple and 3-D FEM detailed. Self inductances, coupling factors, and winding losses are normalized to that obtained with 3-D FEM detailed.

Param.	Sim. 2-D	Sim. 3-D simple	Sim. 3-D detailed
$L_{p,s}$ (%)	94.9	98.7	100.0
k (%)	98.6	101.4	100.0
Losses (%)	103.4	97.1	100.0
Comp. time (s)	3	34	776

B. 3-D FEM Modeling of the Conductive Shielding

The losses in the conductive shielding are computed with 3-D FEM simulations. The model considers aluminum sheets forming a fully closed box around the ACT. The 3-D model takes a third symmetry plane between the coil sets into account to reduce the computational effort. This implies that the model considers the series connections of the coils 2A and 2B on the primary side and of coils 1A and 1B on the secondary side, i.e., there is no cancellation effect of magnetic stray fluxes (see **Fig. 4(a)**). Accordingly, this is a conservative approach that computes increased losses in the shielding (compared to the real setup).

Adding the considered conductive shielding enclosure has minimal effect on the losses in the windings and on the coupling between the primary- and the secondary-side winding (deviation below 1.5 %), i.e., the design of the conductive shielding can be decoupled from the design of the ACT's active part. Therefore, we do not include the modeling of the shielding in the multi-objective optimization; instead, the conductive shielding can be designed afterwards, which opens the possibility for advanced designs that do not require a full enclosure, thus reducing material usage and improving accessibility. **Section IV-C** describes these considerations in detail.

C. Multi-Objective Optimization of the ACT

The multi-objective optimization of the ACT maps the design space given in **Tab. III** to a η-γ-ρ-performance space (efficiency, gravimetric power density, and volumetric power density). Note that the minimum distance between the primary- and the secondary-side windings is fixed to $w_{iso} = 16.5\,\mathrm{mm}$, which follows from the rated isolation voltage of $V_i = 10\,\mathrm{kV}$ and a (conservative, to account for inhomogeneous field distributions, humidity, etc.) maximum permissible electric field of 0.6 kV/mm in air. Note that **Section IV-A** discusses the realization of extended clearance and creepage distances in the actual prototype according to standards by means of added isolation barriers. This, again, can be decoupled from the optimization of the ACT's active part.

During the optimization, which follows [13], a sweep over the following geometrical parameters is carried out, cf. **Fig. 6(a)**:

Copyright (c) 2021 IEEE. Personal use is permitted. For any other purposes, permission must be obtained from the IEEE by emailing pubs-permissions@ieee.org.

This is the author's version of an article that has been published in this journal. Changes were made to this version by the publisher prior to publication.
The final version of record is available at http://dx.doi.org/10.1109/JESTPE.2021.3060506

TABLE III. Design space and constant parameters for the 2-D FEM-based optimization.

Var.	Min.	Max.	# Pts.	Description
f_s	20 kHz	200 kHz	15	operating frequency
N	1	200	200	number of turns
r_i	35 mm	105 mm	15	internal radius
w_1	5 mm	60 mm	15	width of outer coil
w_2	5 mm	60 mm	15	width of inner coil
l	60 mm	700 mm	18	length of coil
Constant parameters				
w_{iso}	16.5 mm			isolation distance
d_{litz}	71 µm			litz strand diameter
k_{litz}	39.5 %			total fill factor of the windings
k_{loss}	30 %			loss penalty due to imperfect twisting

- internal diameter of the inner coil (r_i),
- widths of outer and inner coils ($w_{1,2}$),
- length of coil (l).

For each geometry (60750 in total), the inductances and the coupling are extracted using the 2-D FEM model. Then, considering each geometry, the number of turns (N) and the operating frequency are varied (f_s), and for each of these designs, a model of the entire 1:1-DCX is evaluated to obtain the winding currents, whereby appropriate resonant capacitor values to compensate the calculated leakage inductances must be considered, i.e.,

$$C_{r1} = \frac{1}{(2\pi f_s)^2 L_{\sigma 1}}, \qquad C_{r2} = \frac{1}{(2\pi f_s)^2 L_{\sigma 2}}, \qquad (1)$$

which is in contrast to typical IPT systems, where the respective self inductances are compensated because of the variation of the coupling in case of misalignment [39]. With the winding current waveforms known, the calculation of the ACT losses takes high-frequency effects in the litz wire according to [40], [41] into account, whereby the dimensions of the litz wire for a given design follow from the width of the windings, the number of turns, and the (fixed) strand diameter ($d_{litz} = 71\,\mu m$ and filling factor, $k_{litz} = 39.5\,\%$). Moreover, the calculated losses are increased by 30 % (loss penalty factor k_{loss}) to account for additional losses due to imperfect twisting of litz wires, based on [41], [42]. Transformer designs that exceed a current density of $J_{max} = 20$ A/mm^2 or a surface-related loss density of $p_{v,max} = 0.25$ W/cm^2 are discarded in order to exclude thermally unfeasible designs. The optimization does not consider the weights and volumes of fans, cable terminations, and, as discussed above, the shielding.

Figs. 7(a), **(b)** show the results of the multi-objective optimization of the ACT. The maximum achievable values of the ACT's efficiency (η), the gravimetric power density (γ), and the volumetric power density (ρ) increase if the operating frequency increases. However, a separately conducted overall optimization of the 1:1-DCX, which includes the losses of the SiC MOSFETs, cf. [13], reveals a strong impact of the semiconductor switching losses at high operating frequencies (as experimentally shown in [43], the considered 10 kV SiC MOSFETS show clearly non-

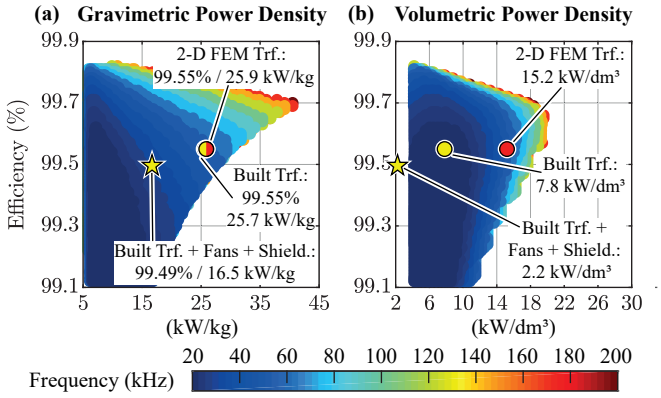

Fig. 7. Results of the multi-objective optimization of the 166 kW / 7 kV transformer, revealing the characteristic dependencies of the η-γ- and η-ρ-Pareto fronts on the operating frequency. The markers highlight the results obtained for the selected design ($f_s = 77.4$ kHz): ● refers to the result obtained with 2-D FEM; ★ and ● represent measured characteristics of the realized prototype with and without the weights and volumes of fans and aluminum conductive shielding, respectively. **(a)** Results for gravimetric power density, γ, versus efficiency; **(b)** results for volumetric power density, ρ, versus efficiency. Note that **Section V-H** provides a detailed comparison of the highlighted design and prototype results.

negligible soft-switching losses). According to the obtained results, the operating frequency must remain below 100 kHz to achieve a system-level efficiency higher than 99.0 %. This constraint together with the availability of only discrete capacitance values of high-power resonant capacitors led us to the selection of a design with an operating frequency of $f_s = 77.4$ kHz, which is highlighted with ● in **Fig. 7**.

In addition to the operating frequency, the selected design defines the geometry of the ACT's active part as well as the number of turns and the dimensions of the litz wire. These values are summarized in the first two sections of **Tab. V**. The following **Section IV** discusses the actual hardware realization of this ACT design in detail.

Note that **Fig. 7** already shows the actually built prototype's locations in the performance space for comparison purposes. However, please refer to **Section V-H** for a detailed comparison between model-based optimization results and measured characteristics of the hardware prototype.

IV. Design and Construction

With the geometry of the ACT's active part identified from the Pareto optimization described in the previous section, certain additional considerations impact the actual mechanical design of the protoype, i.e., the isolation coordination, cooling and airflow, and the practical realization of a suitable conductive shielding. Regarding the overall mechanical arrangement, **Fig. 8(a)** shows how the single-layer winding of each coil is placed on an individual 3D-printed polycarbonate coil former to facilitate the manufacturing.

A. Isolation Coordination

For the optimization, a fixed isolation distance ($w_{iso} = 16.5$ mm) between the primary- and the secondary-side windings has been considered, which ensures safe electrical fields in the air gap between the coils. However, by

Copyright (c) 2021 IEEE. Personal use is permitted. For any other purposes, permission must be obtained from the IEEE by emailing pubs-permissions@ieee.org.

This is the author's version of an article that has been published in this journal. Changes were made to this version by the publisher prior to publication.
The final version of record is available at http://dx.doi.org/10.1109/JESTPE.2021.3060506

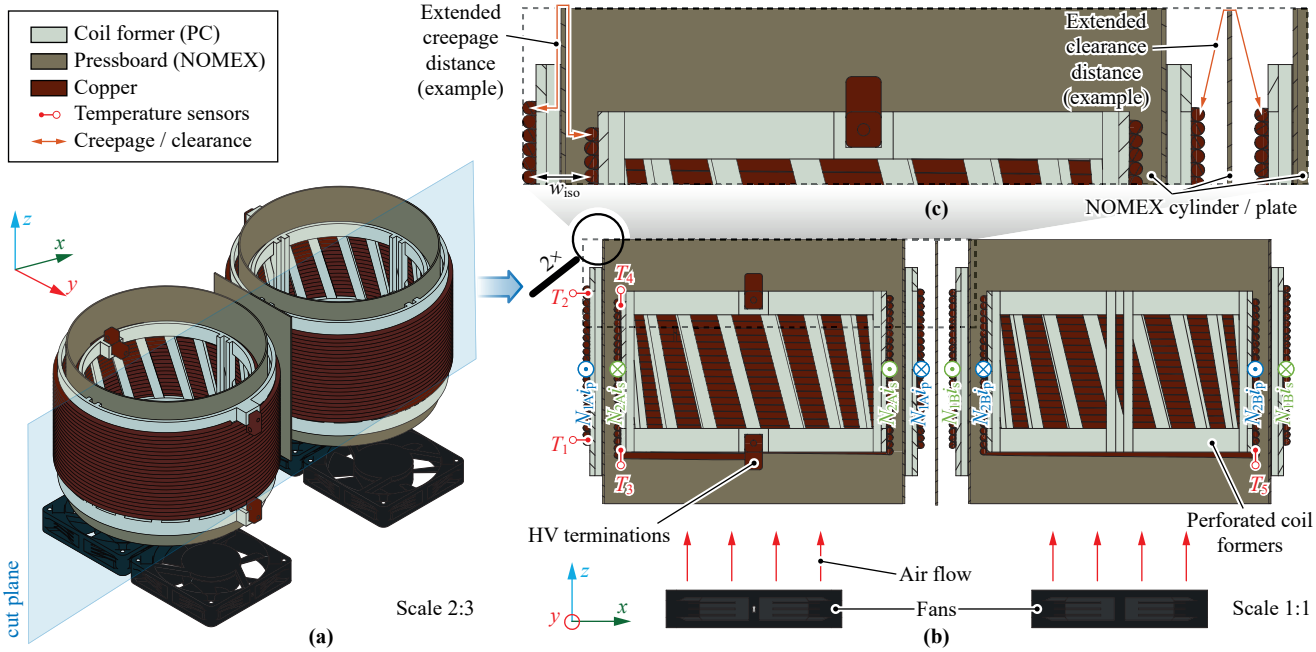

Fig. 8. **(a)** Simplified view of the transformer 3-D model showing windings, terminations, coil formers, insulation barriers, and fans. **(b)** Cut view of the transformer including the flow directions of the currents in the windings, the locations of the temperature sensors, and the direction of the airflow. **(c)** Magnified partial view of the outline of the cross section of the employed insulation concept: required clearance and creepage distances are obtained by placing NOMEX cylinders between coaxial coils and a plate between two sets of coils.

blocking this direct air gap by placing a cylindrical barrier of insulation material (see **Fig. 8**), the effective clearance and creepage distances can be tailored to meet requirements defined in corresponding standards.

We consider a rated DC isolation voltage of $V_\mathrm{i} = 10\,\mathrm{kV}$, i.e., with some reserves over the strict functional requirement of the 7 kV DC bus voltage, and design clearance and creepage distances according to IEC 62477 [44], [45]. The minimum required clearance distance for overvoltage category III (OV-III), which demands an impulse withstand voltage of 37 kV, thus becomes 55 mm. Similarly, the minimum required creepage distance, considering pollution degree 2 (PD2) and isolation material group II, is 71 mm.

In order to realize these clearance and creepage distances, cylindrical barrier elements made of NOMEX pressboards with a thickness of $1.5\,\mathrm{mm}$ are placed between the primary- and secondary-side coils and a rectangular NOMEX plate (thickness of $1.5\,\mathrm{mm}$) is used between the two sets of coils, cf. **Fig. 8(c)**. Both, clearance (66 mm, i.e., corresponding to an impulse withstand voltage of about 43 kV) and creepage (79 mm) could be made longer than the minimum values without compromising other aspects of the mechanical design.

Note that for high-altitude applications (higher than $2\,\mathrm{km}$ above sea level), longer clearance distances are requested by the standard because of the lower air pressure. E.g., the A1 category for airborne equipment according to the DO160 G standard requires operation in environmentally protected (pressurized) zones up to an altitude of $4.6\,\mathrm{km}$ $(15,000\,\mathrm{fts})$, which would require an increase of the clearance distances by a factor of 1.4 according to IEC 62477. In contrast to typical MCTs, the clearance (and creepage) distances of the proposed ACT can be easily extended to meet such requirements by increasing the length of the NOMEX barrier elements. This is supported by the conservative dimensioning of the maximum electric field between the primary-side and secondary-side coils (see **Section III-C**).

For the peak voltage applied to a winding of the transformer, which is the difference of the voltage applied by a half-bridge ($v_\mathrm{p,s}$) and the voltage of the corresponding resonant capacitor ($v_\mathrm{Cr1,Cr2}$), the maximum voltage between two adjacent turns of a coil is only about $5.4\,\mathrm{kV}/44 \approx 123\,\mathrm{V}$, which is well below the capability of the litz wire's insulation, i.e., a double layer of polyamide. The ends of the coils are soldered to copper block terminations which are edgeless (i.e., feature rounded edges) to prevent excessive local electric fields in the surrounding air.

B. Cooling and Airflow

To improve the thermal design of the windings, the walls of the coil formers are perforated (similar to a squirrel cage rotor), in order to increase the winding's surface that is directly exposed to the airflow (see **Fig. 8(b)**). The fans are placed below the transformer. Thus, the airflows due to forced cooling and natural convection have the same direction, which opens the possibility of passive cooling at light load.

C. Optimized Conductive Shielding

As discussed earlier, the presence of a conductive shielding enclosure does not affect the ACT's coupling or winding losses. Therefore, the shielding can be designed in a second step, whereby the mass (and hence the volume) of the enclosure is minimzed conditional on sufficient distance from the coils and the required interconnections, considering

Copyright (c) 2021 IEEE. Personal use is permitted. For any other purposes, permission must be obtained from the IEEE by emailing pubs-permissions@ieee.org.

This is the author's version of an article that has been published in this journal. Changes were made to this version by the publisher prior to publication.
The final version of record is available at http://dx.doi.org/10.1109/JESTPE.2021.3060506

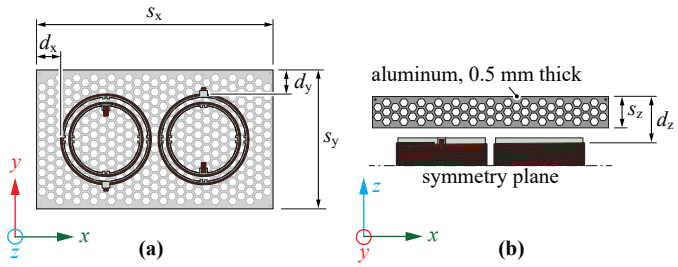

Fig. 9. Simplified 3-D CAD model of the transformer, showing windings, coil formers, terminations, and conductive aluminum shielding featuring a honeycomb pattern of holes: **(a)** top view, **(b)** side view. Projections are in scale and main mechanical dimensions are shown.

TABLE IV. Specifications of the conductive aluminum shielding.

Dimensions of shielding		
d_x	60.5 mm	distance from coils in x-axis
d_y	60.5 mm	distance from coils in y-axis
d_z	126.0 mm	distance from coils in z-axis
s_x	601 mm	width of shielding
s_y	353 mm	depth of shielding
s_z	80 mm	height of shielding
t_{sh}	0.5 mm	thickness of shielding

clearance/creepage distances, and low losses ($< 10\,\%$ of the total losses). This is an iterative process aided by the 3-D FEM simulations described in **Section III-B**.

However, whereas the FEM-based design considers a fully closed box, this would limit the accessibility of the coils. Thus, to facilitate access to the windings and simplify experimental testing, we realize a partial shielding, which is composed of a bottom part and a top part only (i.e., the walls on the sides are omitted), instead of a full enclosure. **Fig. 9** shows one part of the designed shielding and **Tab. IV** lists the corresponding dimensions. FEM simulations shown in **Fig. 10** reveal that the top and bottom of the ACT are critical regarding external stray fields (see **Fig. 10(a)**), and that the selected partial shielding provides the required shielding efficacy in these locations (see **Fig. 10(b)**). In addition, **Fig. 10(c)** indicates that a full enclosure further improves the shielding effect. Therefore, measuring the external stray fields of a prototype with partial shielding (see **Section V-G**) is a conservative approach, which further confirms its suitability for testing purposes. Also, the partial shielding configuration is conservative with regard to losses, since it overestimates the total losses in the shielding by a factor of 1.8 compared to a complete enclosure. The increased losses in the partial shielding can be explained by a crowding of the eddy currents close to the edges (i.e., especially on the sides where the partial shielding ends, and where a full enclosure would provide additional area for the eddy currents to flow), thus leading to areas with a high local current density and hence losses.

Furthermore, a full enclosure made of solid sheet-metal would complicate forced-air cooling. Thus, we perforate the shield in a honeycomb pattern (cf. **Fig. 9**), achieving also a decrease of the weight of the shielding by $30\,\%$. With this, the shielding efficacy remains sufficiently high, however, the

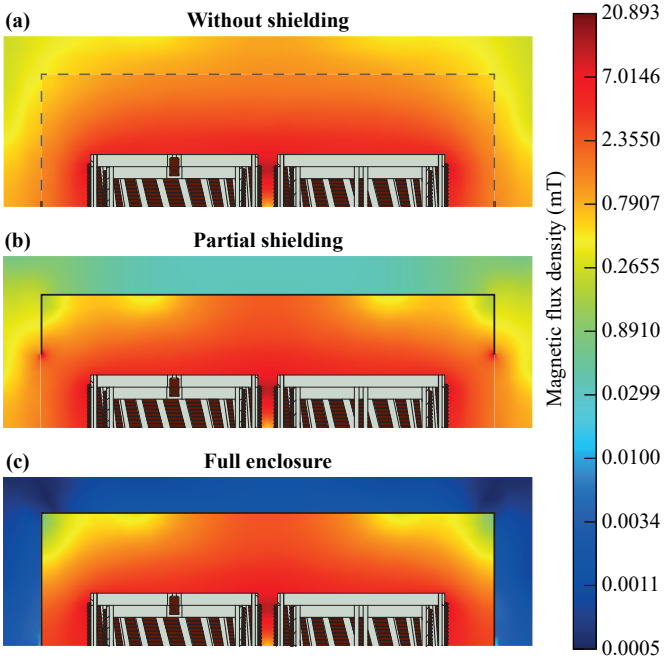

Fig. 10. FEM-simulated flux densities with nominal primary- and secondary-side currents (cf. cut plane defined in **Fig. 5**): **(a)** ACT without shielding; **(b)** partial shielding as employed in the prototype to facilitate access to the windings; **(c)** full enclosure. The shielding is modeled without honeycomb pattern. Note the logarithmic color scale.

losses in the shielding increase by $29\,\%$ (compared to non-perforated shielding); essentially because similar shielding efficacy implies similar circulating eddy currents, which generate higher losses because of the reduced cross-sectional area.

D. Resulting Prototype

Fig. 11 depicts the realized MV/MF ACT of the 1:1-DCX and **Tab. V** summarizes its dimensions and key design parameters. Acrylic glass plates with slots are inserted from the top and the bottom of the coils (along the z-axis, cf. **Fig. 11(a)**), to fix the positions of all components, including the fans and the partial top- and bottom-side shielding. In the following section we describe the experimental methodology and provide detailed measurement results to characterize the prototype's performance.

V. Experimental Setup and Results

This section summarizes the experimental characterization of the ACT prototype shown in **Fig. 11**, including a variety of measurements, e.g., small-signal impedance measurements, large-signal tests, loss measurements, transient thermal responses, magnetic stray flux densities (without and with shielding), and insulation tests. The results provide further validation of the employed models described in **Section III**.

As a preliminary remark, note that several measurement approaches make use of an important property of an ACT: its linearity. As there is no core material, there are no saturation phenomena, i.e., the ACT's key properties such as coupling,

Copyright (c) 2021 IEEE. Personal use is permitted. For any other purposes, permission must be obtained from the IEEE by emailing pubs-permissions@ieee.org.

This is the author's version of an article that has been published in this journal. Changes were made to this version by the publisher prior to publication.
The final version of record is available at http://dx.doi.org/10.1109/JESTPE.2021.3060506

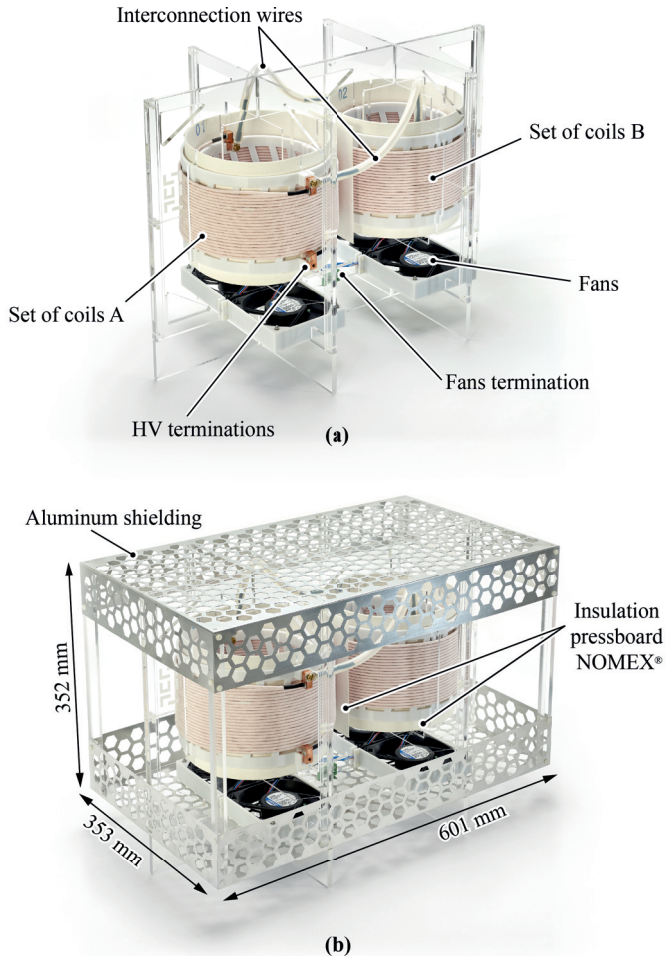

Fig. 11. Photo of the realized 166 kW / 7 kV air-core transformer (ACT): **(a)** without shielding, **(b)** with aluminum conductive shielding.

TABLE V. Key characteristics of the realized 166 kW / 7 kV air-core transformer (ACT) prototype and the resonant capacitor bank.

Air-Core Transformer		
r_i	90 mm	internal radius, cf. Fig. 6(a)
w_1	4.5 mm	width of outer winding
w_2	4.5 mm	width of inner winding
l	98.6 mm	length of coil
Winding		
N	2×22	number of turns (single layer)
Litz wire	$5 \times 10 \times 40$	strands in 3 bundle levels (total of 2000 strands)
	double layer polyamide	outer insulation of litz wire
d_litz	71 µm	single strand diameter
n_litz	2000	number of strands
J_litz	7.2 A/mm^2	current density
Equivalent circuit parameters		
$L_{\sigma 1,2}$	51.8 µH	primary / secondary leakage inductance
L_m	162.6 µH	magnetizing inductance
n	1 : 1	transformer turns ratio
k	0.76	coupling factor
$I_\mathrm{p,s}$	56.6 A	primary / secondary transformer rms current
I_m	40.0 A	magnetizing rms current
Isolation		
V_i	10 kV	DC isolation voltage
d_clear	66 mm	clearance distance
d_creep	79 mm	creepage distance
Resonant capacitor bank		
f_s	77.4 kHz	operating frequency
$C_{\mathrm{r}1,2}$	81.6 nF	input / output side resonance capacitance

inductances, and AC resistances do not directly depend on current and voltages (not considering thermal effects).

Note that the ACT is placed on a wooden table (i.e., without metal legs) and the used measurement equipment (i.e., its active parts) is placed at sufficient distance (> 1 m) to prevent interactions of the ACT's fields with nearby metal parts.

A. Impedance Measurements

To validate the computed values of $L_{\sigma 1,2}$ and L_m from the equivalent circuit of **Fig. 5,** the short-circuit and open-circuit impedances are measured with an Agilent 4924A precision impedance analyzer from the primary and from the secondary side (without the shielding present). Moreover, the common-mode (CM) impedance across the galvanic insulation is measured between the shorted primary-side winding and the shorted secondary-side winding. **Fig. 12** shows the obtained results and **Tab. VI** compares the simulated and the measured values of the equivalent circuit parameters (at a frequency of 77.4 kHz). All deviations between measurements and simulations are below 16 %. The CM capacitance is relatively low and equal to 102 pF. Furthermore, all resonance frequencies are much higher than the operating frequency and are found to be uncritical with regard to the operation of the 1:1-DCX [46].

B. Large-Signal Tests

Large-signal tests of the ACT could be conducted in the course of an experimental test of the entire 1:1-DCX, cf. **Fig. 2(a)**, which, however, requires two fully operational MV/MF half-bridges. Each of the half-bridges needs to process the rated power of 166 kW and allow for operation with $f_\mathrm{s} = 77.4$ kHz. To circumvent the costs and uncertainties related to the realization and operation of such 10 kV half-bridge converters, an alternative approach is pursued in this paper. Since the currents in the ACT of the 1:1-DCX are quasi-sinusoidal (cf. **Fig. 2b**), the ACT can be operated in a series resonant circuit that is supplied by a power amplifier, instead. This effectively emulates power operation. Note that since the ACT is not subject to core losses and is a linear device, large-signal validation can be done with scaled voltages/currents, i.e., operation at rated current is not necessary.

TABLE VI. Small-signal parameters of the ACT (without shielding, determined at $f = 77.4$ kHz).

Param.	Sim. 2-D	Sim. 3-D	Meas.	Dev. 2–D \ 3-D
$L_{1,2}$	204.5 µH	214.2 µH	214.4 µH	4.6 % \ 0.1 %
L_m	144.4 µH	155.9 µH	162.6 µH	11.2 % \ 4.2 %
$L_{\sigma 1,2}$	60.1 µH	58.4 µH	51.8 µH	16.0 % \ 12.6 %
k	0.706	0.728	0.758	7.4 % \ 3.8 %

Copyright (c) 2021 IEEE. Personal use is permitted. For any other purposes, permission must be obtained from the IEEE by emailing pubs-permissions@ieee.org.

This is the author's version of an article that has been published in this journal. Changes were made to this version by the publisher prior to publication.
The final version of record is available at http://dx.doi.org/10.1109/JESTPE.2021.3060506

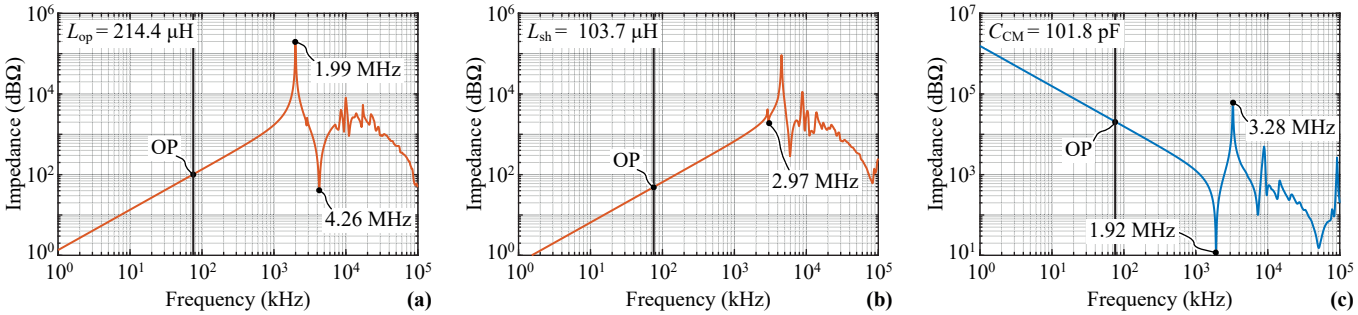

Fig. 12. Measured frequency characteristics of selected impedances of the transformer (without shielding): **(a)** primary-side impedance for open secondary-side winding; **(b)** primary-side impedance in case of a secondary-side short-circuit; **(c)** CM impedance between shorted primary-side and shorted secondary-side windings. The impedance values corresponding to the operating frequency (77.4 kHz) are marked with a black dot (operating point, OP). Additionally, different resonance frequencies are labeled.

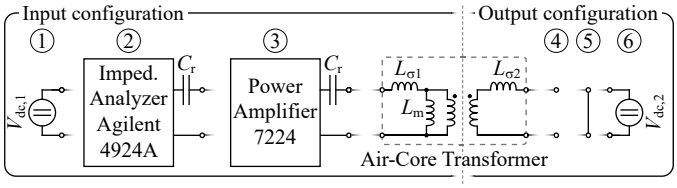

Fig. 13. Input devices and output configurations of the different measurement circuits. ① DC source for thermal calibration, ② impedance analyzer with series resonant capacitor for small-signal measurements of AC resistances, ③ power amplifier with series resonant capacitor for large-signal measurements. Depending on the measurement, either an open-circuit ④ or a short-circuit ⑤ is realized at the secondary side. The last configuration, with a secondary-side DC source ⑥, is used for the thermal calibration only.

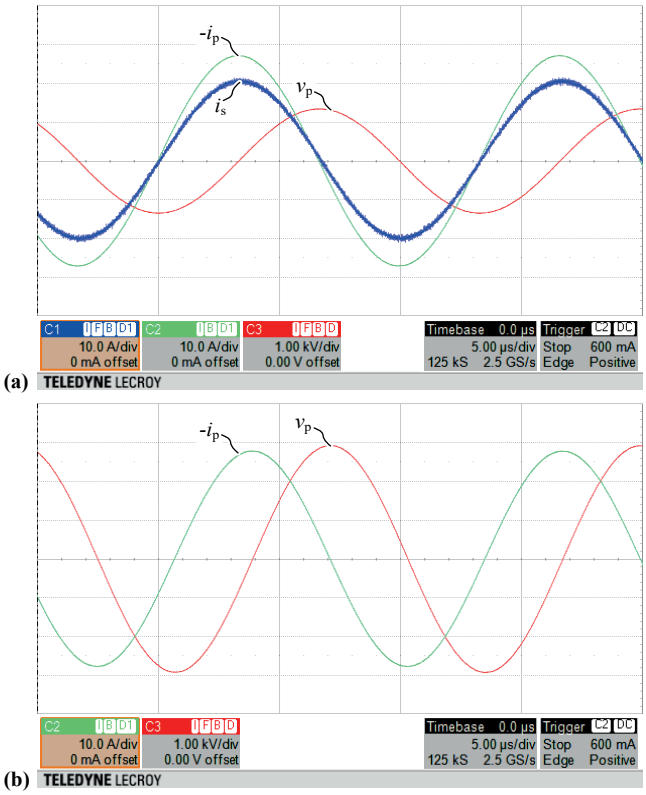

Fig. 14. Voltage and current waveforms measured in the course of the large-signal tests that utilize series resonant operation. **(a)** Secondary-side short-circuit (rms values): primary-side current is 19.6 A, primary-side voltage is 0.93 kV, secondary-side current is 14.6 A, and resonance frequency is 75.3 kHz. **(b)** Secondary-side open-circuit (rms values): primary-side current is 19.9 A, primary-side voltage is 2.04 kV, and resonance frequency is 78.0 kHz.

Fig. 13 gives an overview of the different input and output configurations used to assess the ACT. With regard to the large-signal test at scaled current, the input configuration ③ is used, i.e., an AE Techron 7224 power amplifier with a capacitor connected in series. This resonant capacitor C_r is realized as a high-power polypropylene capacitor bank (CELEM CSP120/200) and the series resonance frequency is set to approx. f_s. The transformer currents are measured with a Pearson 110A current probe and a LeCroy HDO4054A 12-bit oscilloscope. The current measurement is subject to a total uncertainty of $+2\,\%$ / $-1\,\%$.

Fig. 14(a) shows the result of the test with a secondary-side short-circuit (output configuration ⑤), which reveals a secondary-side rms current of 14.6 A for a primary-side rms current of 19.6 A. This result agrees well with the expected secondary-side current of 14.8 A (for $k = 0.76$ as obtained from the impedance analyzer measurements described above, cf. **Tab. VI**).

The same setup can be used to assess the self inductance of the ACT; in this case, the secondary-side winding is left open (output configuration ④). **Fig. 14(b)** presents the measurement results, with a primary-side rms voltage of 2.04 kV, a primary-side rms current of 19.9 A, and a phase shift of 90°. This corresponds to a self inductance of 209 µH, which corroborates the impedance analyzer measurement, see **Tab. VI**.

The close agreement of the coupling and inductances values measured with an impedance analyzer (i.e., small-signal) and with a power-amplifier-based setup (i.e., large-signal) confirms that the ACT is a linear system.

C. AC Resistances of the Windings

The measurement of the coils' AC resistances is a challenging task, due to their high quality factors ($Q \geq 1000$), which complicates electrical measurements, and because of the large volume of the ACT ($75\,\mathrm{dm}^3$) that renders steady-state calorimetric approaches impractical.

1) Impedance analyzer: However, as the ACT is a linear system, a direct measurement of the AC resistances

Copyright (c) 2021 IEEE. Personal use is permitted. For any other purposes, permission must be obtained from the IEEE by emailing pubs-permissions@ieee.org.

This is the author's version of an article that has been published in this journal. Changes were made to this version by the publisher prior to publication.
The final version of record is available at http://dx.doi.org/10.1109/JESTPE.2021.3060506

TABLE VII. Comparison of FEM-simulated AC resistances with measurement results obtained with an impedance analyzer with a series resonant compensation, cf. input configuration ② in **Fig. 13**. In the short-circuit case, R_{AC} is the sum of *both* winding's AC resistances, referred to the primary side. Note that the operating frequencies do not exactly match the nominal value because only discrete capacitance values are available to realize the series compensation capacitor.

Param.	Sim. 3-D	Measurement	
		w/o Shield.	w/ Shield.
Open Circuit		**@ 79.0 kHz**	**@ 80.5 kHz**
R_{AC}	72.4 mΩ	116.3 mΩ (dev. 60.6 %)	182.9 mΩ
Short Circuit		**@ 79.0 kHz**	**@ 79.8 kHz**
R_{AC}	114.3 mΩ	172.0 mΩ (dev. 50.5 %)	192.9 mΩ

with an impedance analyzer is possible, at least in theory. Unfortunately, the high reactive component of the coil's impedance leads to a very inaccurate measurement of the resistive component, which renders the result of the direct measurement unusable. In order to avoid its unwanted impact, the reactance of the tested coil can be compensated at the measurement frequency. For this purpose, a high quality capacitor with very low losses is connected in series (input configuration ② in **Fig. 13**; MLCC C0G *Knowles High Q* capacitors have been used for C_{r}). Still, the measured primary-side AC resistances for secondary-side open- and short-circuits are 60.6 % and 50.5 % higher than the resistances computed with the corresponding 3-D FEM simulations, respectively, cf. **Tab. VII** (without considering a loss-correction factor k_{loss}, cf. **Tab. III**, to account for imperfect twisting observed in practical litz wires, see **Sec. V-D** below). This indicates a significant impact of the capacitor's equivalent series resistance on the total resistance and limits the measurement method to applications where a *change* of the resistance is assessed, e.g., when evaluating the AC resistances without and with the shielding present to determine the losses in the shielding, see **Section V-G**.

2) Transient calorimetric: Alternatively, a transient calorimetric method can be used to measure the AC resistance, which is a two-step procedure that relies on measuring the winding temperatures over time. To do so, two types of sensors are placed between the first two turns and the last two turns of the coils at the five positions marked with $T_{\{1,2,3,4,5\}}$ in **Fig. 8(b)**. NTC sensors (PS104J2 thermistor) are used during thermal tests with DC currents; however, due to the lack of isolation, only one NTC sensor, T_1, can be used during AC tests because of the significantly higher voltage levels. Thus, fiber optic sensors (FOTEMPMK-19 Modular) are used to measure $T_{\{1,2,3,4,5\}}$ during AC tests.

Firstly, DC currents are injected into the windings in order to determine the step responses of all measured temperatures for given losses in the windings (in the range of 10 W to 40 W). In this context, one DC source is used if a secondary-side open-circuit is assessed (input configuration ① in **Fig. 13**) and two DC sources if a secondary-side short-circuit is evaluated (input and output configurations ① and ⑥ in **Fig. 13**, respectively). **Fig. 15(a)** presents example step responses of the temperature sensor T_1 (cf. **Fig. 8(b)**) for four different values of power being dissipated in the primary-side coils. In this measurement, the secondary side

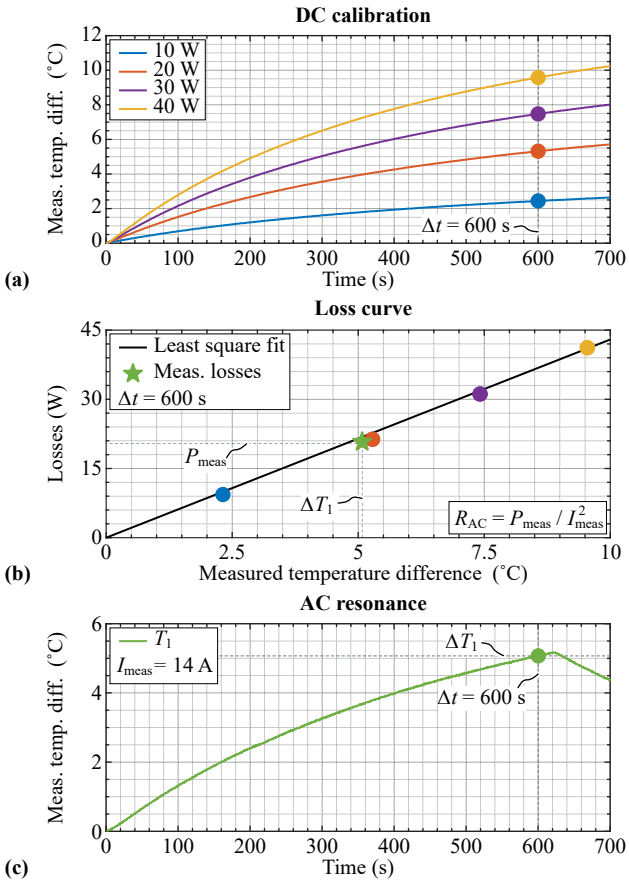

Fig. 15. Transient calorimetric measurement of the AC resistance—exemplary illustration of the processing of the measured step responses of temperature sensor T_1 and for a secondary-side open-circuit of the ACT: **(a)** initial measurements of the temperature step responses for defined losses on the primary side, ranging from 10 W to 40 W; **(b)** linear approximation of the dependency of the temperature increase, $\Delta T_1(\Delta t = 600\,\mathrm{s}) = T_1(\Delta t) - T_1(0)$, on the losses; the slope of this function is computed with a least squares optimization; **(c)** final measurement of the step response of T_1 for a primary-side AC rms current of 14 A.

of the ACT has been left open. The obtained step responses enable the compilation of a loss-vs.-temperature characteristic for each temperature sensor, which relates the losses to a measured temperature increase after a defined time, Δt. **Fig. 15(b)** depicts the loss curve that results for the transient temperature waveforms of **Fig. 15(a)**, i.e., for temperature sensor T_1 and a secondary-side open-circuit, and $\Delta t = 600\,\mathrm{s}$.

Subsequently to this initial calibration, the ACT is operated in AC resonance (using a power amplifier and series compensation capacitor, see **Section V-B**) with a defined primary-side current, I_{meas}. After the time interval Δt has elapsed (cf. **Fig. 15(c)**), the temperature increase measured by each temperature sensor together with the corresponding calibration data for that sensor allows to determine the winding losses (cf. **Fig. 15(b)**). Finally, the AC resistance is calculated as $R_{\mathrm{AC}} = P_{\mathrm{meas}}/I_{\mathrm{meas}}^2$. The uncertainties of the temperature measurements with the high-precision NTC sensors and the fiber optic sensors are ±0.1 °C and ±0.2 °C, respectively, which corresponds to loss deviations of ±0.4 W and ±0.8 W and resistance deviations of ±2 mΩ and ±4 mΩ, respectively (for a measurement current of 14 A). The maximum uncertainty of the current measurement

Copyright (c) 2021 IEEE. Personal use is permitted. For any other purposes, permission must be obtained from the IEEE by emailing pubs-permissions@ieee.org.

This is the author's version of an article that has been published in this journal. Changes were made to this version by the publisher prior to publication.
The final version of record is available at http://dx.doi.org/10.1109/JESTPE.2021.3060506

is $+2\,\%/-1\,\%$, cf. **Section V-B**, which corresponds to an additional uncertainty of the measured R_{AC} of $+2\,\%/-4\,\%$, e.g., $+2\,\mathrm{m\Omega}/-4\,\mathrm{m\Omega}$ for a typical $P_{\mathrm{meas}} = 20\,\mathrm{W}$ and a measurement current of 14 A (corresponding to an R_{AC} of about $100\,\mathrm{m\Omega}$).

Tab. VIII lists the results of the conducted measurements. The final AC resistances are calculated by averaging the values obtained from different temperature sensors and are listed in **Tab. IX** together with the results of corresponding FEM simulations. Note that the transient calorimetric method enables individual measurements of the AC resistances of the primary and of the secondary-side winding also for a shorted secondary-side winding (in contrast to the small-signal approach discussed earlier). It can be seen that the transient calorimetric method allows to measure the AC resistance more accurately than the small-signal method (cf. **Tab. VII**), however the deviations to the simulated values ($25\,\%$ to $40\,\%$, without applying the loss-correction factor k_{loss} to the FEM results) are still high. A likely reason for this is imperfect twisting of the litz wire, which is known to cause increased winding losses [41], [42] and is thus investigated in the next section.

D. Litz Wire Current Sharing

The current sharing in the bundles of the used litz wire is analyzed in order to determine whether the measured increase of the AC resistance above the values expected from simulations may be caused by imperfect twisting. The litz wire used in the transformer consists of 2000 strands with a single-strand diameter of $71\,\mu\mathrm{m}$. It is twisted in 3 levels: top-level (5 bundles), mid-level (10 subbundles) and strand-level (40 strands), see **Fig. 16(a)**. To examine the current sharing, a test coil with an inner diameter of $160\,\mathrm{mm}$ and 31 turns (single layer, total length of $51\,\mathrm{cm}$) is wound, i.e., the test coil has similar dimensions as one of the ACT's coils. Its litz wire has been partially untwisted to have access to all bundles and, in addition, one of the subbundles (No. 5) has been untwisted to have access to all of its strand-level bundles. **Figs. 16(b), (c)** depict the measured currents flowing in the individual bundles and subbundles, respectively, for a total rms current of $0.6\,\mathrm{A}$ at a frequency of $80\,\mathrm{kHz}$. The amplitudes of the currents flowing in the top-level bundles deviate on average by 23.2 % from the ideal values in case of symmetric current sharing, and the phase-shifts are rather small (between -2 ° and 5 °). In bundle No. 5, i.e., on the middle level, the amplitudes deviate on average by 18.4 %, and the phase-shifts are larger, i.e., between -18 ° and 55 °. Thus, the current sharing among bundles, and within a bundle among the subbundles is clearly not symmetric, confirming a non-ideal twisting scheme of

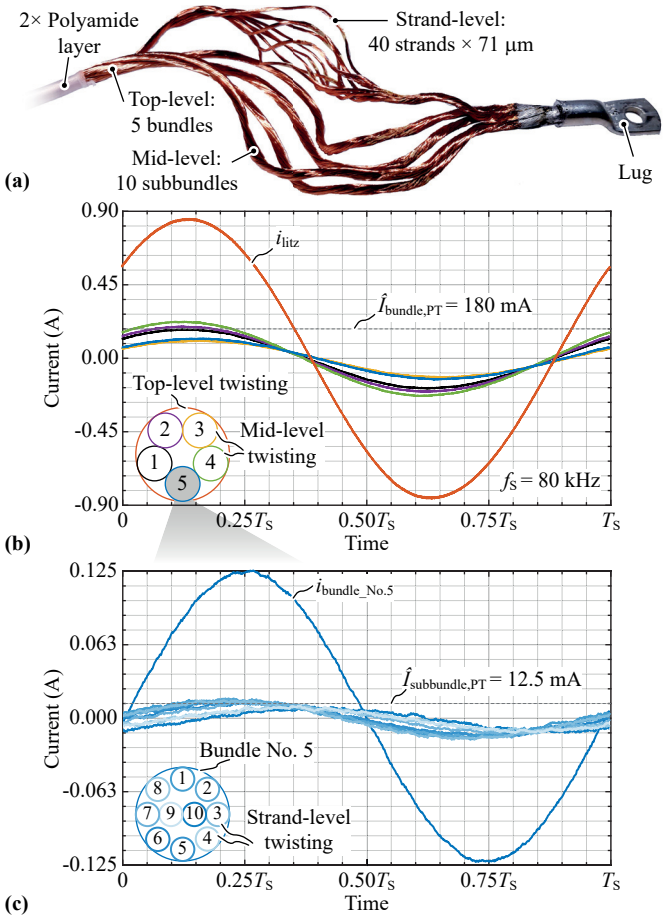

Fig. 16. **(a)** Photo of the litz wire ($5 \times 10 \times 40$ strands with single-strand diameter of $71\,\mu\mathrm{m}$) being prepared for current sharing measurements. **(b)** Current sharing in the five top-level bundles; **(c)** current sharing in the ten mid-level subbundles of bundle No. 5. The total current in the litz wire, I_{litz}, is $600\,\mathrm{mA}$. For reference, the peak values of the currents in the bundles of a hypothetical, perfectly twisted litz wire are shown on top level ($\hat{I}_{\mathrm{bundle,PT}}$) and middle level ($\hat{I}_{\mathrm{subbundle,PT}}$).

TABLE VIII. Results of the transient calorimetric method for the measured AC resistances.

Sensor	ΔT (°C)	P (W)	I_{p} (A)	I_{s} (A)	$R_{\mathrm{AC,1}}$ (Ω)	$R_{\mathrm{AC,2}}$ (Ω)
Open-circuit						
T1 (NTC)	5.0	20.5			104.4	-
T1 (OPT)	5.3	19.5	14.0	-	99.5	-
T2 (OPT)	4.9	20.0			101.9	-
Short-circuit						
T1 (NTC)	4.0	17.2			95.4	-
T1 (OPT)	4.3	17.3			95.9	-
T2 (OPT)	4.0	17.2	13.4	10.2	95.0	-
T3 (OPT)	3.5	16.8			93.2	-
T5 (OPT)	2.9	10.2			-	97.5

NTC - PS104J2 thermistor
OPT - fiber optic thermometer FOTEMPMK-19 Modular

TABLE IX. Comparison of FEM-simulated AC resistance values against the results obtained through transient calorimetric measurements. Note that the operating frequencies do not exactly match the nominal value because only discrete capacitance values are available to realize the series compensation capacitor, cf. input configuration ③ in **Fig. 13**.

Param.	Sim. 3-D	Meas.	Deviation
Open Circuit @ 80 kHz / 14.0 A			
$R_{\mathrm{AC,1}}$	72.4 mΩ	101.9 mΩ	40.8 %
Short Circuit @ 75.3 kHz / 13.4 A			
$R_{\mathrm{AC,1}}$	69.5 mΩ	95.4 mΩ	37.3 %
$R_{\mathrm{AC,2}}$	77.9 mΩ	97.5 mΩ	25.1 %

Copyright (c) 2021 IEEE. Personal use is permitted. For any other purposes, permission must be obtained from the IEEE by emailing pubs-permissions@ieee.org.

This is the author's version of an article that has been published in this journal. Changes were made to this version by the publisher prior to publication.
The final version of record is available at http://dx.doi.org/10.1109/JESTPE.2021.3060506

the litz wire [42].

To quantitatively assess the impact of this imperfect twisting on the coil's AC resistance, the losses in the investigated test litz wire are compared with losses in a hypothetical, perfectly twisted one. The analysis is based on the assumption that the current sharing in the subbundles of all bundles is the same as measured in bundle No. 5; this is a valid assumption because all top-level bundles are of identical internal structure. The corresponding computation reveals an increase of the AC resistance by 24 %, which explains the largest part of the deviations between the AC resistances obtained from (transient-calorimetric) measurements and FEM simulations (not yet considering the loss penalty factor k_{loss}), cf. **Tab. IX**. The remaining deviation may be related to uncertainties of the computed fields, further imperfections of the litz wires, or resistances of terminations. Furthermore, this result justifies the value of the loss penalty factor used in the optimization, $k_{loss} = 30\,\%$, which had been selected *a priori* based on literature and experience [41], [42].

E. Thermal Tests

To verify the thermal feasibility of the transformer, heat runs are carried out considering two different operating conditions, i.e., nominal operation with active cooling ($4\times12\,\mathrm{W}$, 4414FNH fans) and maximum allowable transformer power without overheating in case of passive cooling. We emulate these operating conditions using high DC currents, i.e., we employ a DC source that injects a current into the series connection of primary- and secondary-side windings of the ACT. The current is selected based on the ratio of AC to DC resistances ($R_{\mathrm{AC}}/R_{\mathrm{DC}} = 1.48$ @ $30\,^{\circ}\mathrm{C}$) such that the losses expected for operation with AC currents are generated.

Fig. 17 shows the thermal images of the prototype and the evolution of measured temperature waveforms during the heat runs. Note that even though the litz wire features temperature class V155, the maximum allowable temperature is $T_{\mathrm{max}} = 130\,^{\circ}\mathrm{C}$ due to the thermal stability of the outer polyamide insulation [47]. During rated operation, the hotspot reaches 103 °C at an ambient temperature of 25 °C, cf. **Fig. 17(a)** and ① in **Fig. 17(b)**, which leaves a margin of $\Delta T = 27\,^{\circ}\mathrm{C}$ to T_{max}, or, alternatively, would allow operation at ambient temperatures of up to about 50 °C.

Furthermore, the transformer can operate with passive cooling (e.g., in case the fans would fail) up to approximately 420 W of losses, cf. **Fig. 17(c)** and ② in **Fig. 17(b)**. This corresponds to operation at an output power of 117 kW (70 % rated output power).

Finally, the thermal time constants of the ACT with and without fans can be extracted from **Fig. 17** as 3.2 min and 5.2 min, respectively, which are several times shorter than for high-power MF MCTs [16], [46].

F. Insulation and Voltage Withstand Tests

To test the insulation of the transformer, first, the DC isolation resistance between primary and secondary side, i.e., common-mode insulation, is measured with an insulation tester (Megger MIT410, DC test voltage of 1 kV). The measured insulation resistance is greater than 100 GΩ, which corresponds to a leakage current of less than 70 nA for a voltage of 7 kV. This isolation resistance is more than a hundred times higher than the specified values [48], [49]. Additionally, the same insulation has been successfully tested at higher voltages, with a Schleich GLP2 voltage tester (for 1 min each): +9.6 kV (DC), −9.6 kV (DC), and 6.36 kV (rms) at $f = 50\,\mathrm{Hz}$. In summary, those tests indicate that the realized prototype withstands the rated isolation voltage.

G. Magnetic Fields and Shielding

1) Shielding losses: The losses in the conductive shielding are directly related to the difference of the AC resistances that are measured with and without shielding. Accordingly, the small-signal setup described in **Section V-A** can be used for this purpose. **Tab. VII** lists the measurement results and reveals an increase of the AC resistance by 12 % (short-circuit test, i.e., all coils carry current). This corresponds to 92 W of losses in the tested conductive shielding, which covers only the top and bottom parts. Using FEM results to scale this measurement to a full enclosure (made of aluminum sheet metal with a honeycomb pattern of openings) results in 50 W of expected losses, cf. **Section IV-C** for an explanation for these lower losses in case of a full enclosure.

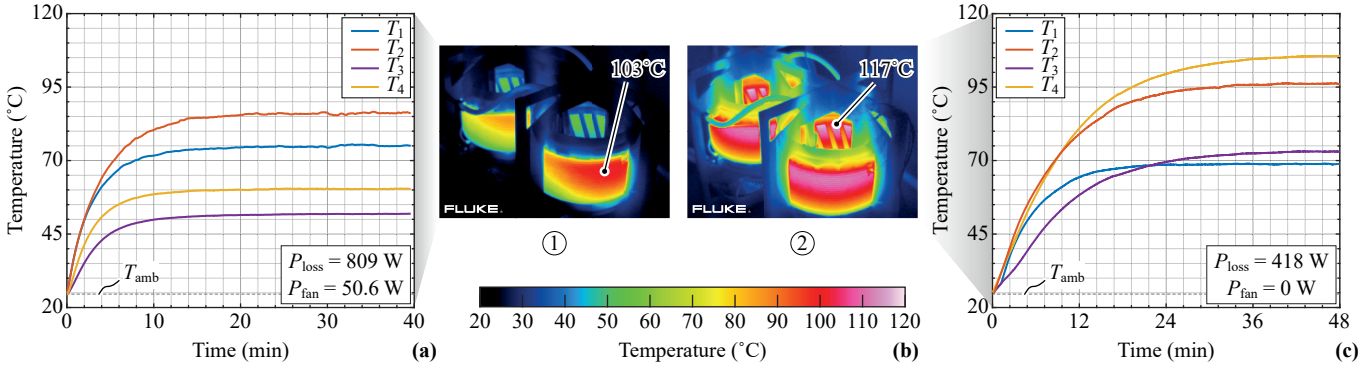

Fig. 17. Temperatures measured with four PS104J2 NTC thermistors, $T_{1\ldots4}$, placed in the windings (cf. **Fig. 8(b)**), for **(a)** a nominal load step with nominal cooling and **(c)** a maximum allowable load step ($P_{\mathrm{passive}} \cong 0.7 \cdot P_{\mathrm{N}}$) with passive cooling (derating in case of fan failure). **(b)** Corresponding thermal images with labeled hotspots of the ACT during two load step tests: ① nominal operation, ② allowable load with passive cooling.

Copyright (c) 2021 IEEE. Personal use is permitted. For any other purposes, permission must be obtained from the IEEE by emailing pubs-permissions@ieee.org.

This is the author's version of an article that has been published in this journal. Changes were made to this version by the publisher prior to publication.
The final version of record is available at http://dx.doi.org/10.1109/JESTPE.2021.3060506

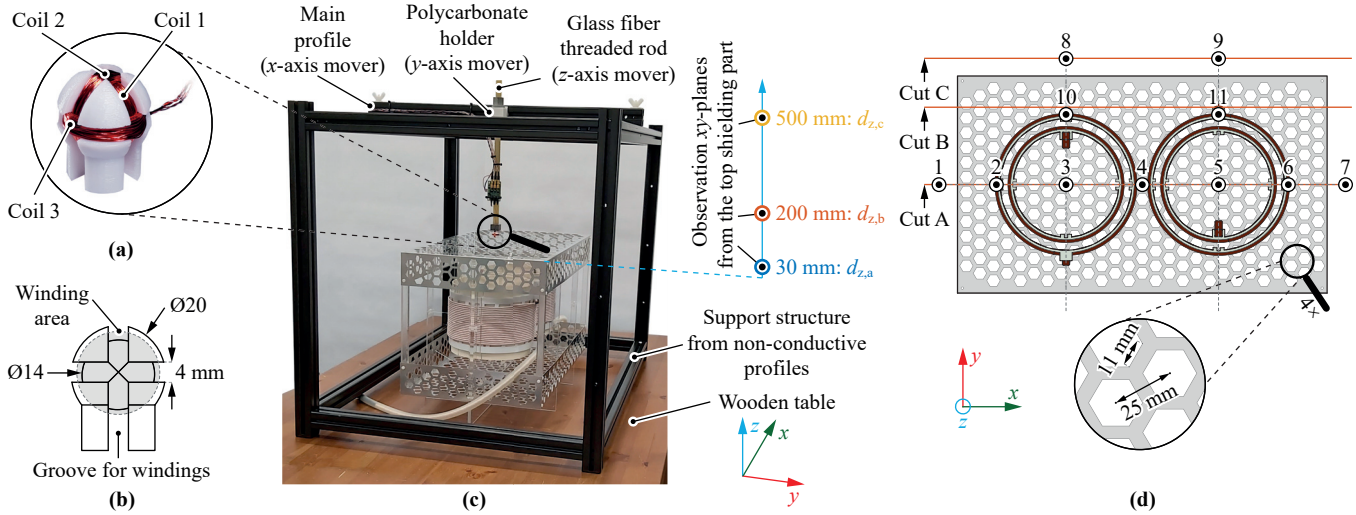

Fig. 18. **(a)** Picture and **(b)** CAD drawing of the field probe that is used to measure the magnetic flux density. A 3-D-printed polycarbonate sphere is used to support three coils with 50 turns each. **(c)** Picture of the measurement setup used to achieve a precise positioning ($\pm$ 1 mm) of the field probe in x-, y-, z-directions. Additionally, the distances in z-direction, $d_z = d_{z,\{a,b,c\}}$, between the top surface of the shielding and the plane containing the observation points for the measurements are shown. **(d)** Top view of the transformer; the points 1 to 11 mark the locations of the observation points in the xy-plane.

Considering the large surface area of the shield A_s and a conservative heat transfer coefficient for natural convection of $h_c = 5\,\mathrm{W/m^2K}$, the shield's temperature rise follows from a simplified calculation as approximately $T_s = 50\,\mathrm{W}/(h_c \cdot A_s) = 13\,\mathrm{K}$. In practice, the heat transfer coefficient would be significantly higher because of the fans (forced convection). Therefore, it can be concluded that the heating of the shielding due to the induced eddy currents is negligible.

Note that the change of the AC resistance for open-circuit tests (60 %) is larger, because there is no current in the secondary-side winding that would have a canceling effect on the magnetic stray flux outside of the ACT, see **Section II-B**.

2) Stray fields without shielding: The FEM-based predictions of the magnetic stray flux densities in the vicinity of the ACT and the efficacy of the shielding are experimentally verified using a custom-made magnetic field probe. The implemented field probe measures the induced voltage at the design frequency of 80 kHz and is constructed similarly to the probe presented in [50]. For the measurement of three spatial components of the magnetic flux density vector, three sensor windings are arranged perpendicularly on a 3-D printed spherical support made from polycarbonate, as shown in **Fig. 18(a)**; **Fig. 18(b)** depicts the dimensions of the spherical support. Each winding consists of 50 turns to achieve a sensitivity of approx. $0.75\,\mathrm{mV/\mu T}$. The output signal of the built field probe has been compared to that of a commercial field probe (MC162 by *Magnetic Sciences Inc.*), confirming deviations of less than 3 %.[1] The custom-made positioning setup depicted in **Fig. 18(c)** enables a precise positioning of the field probe in x-, y-, and z-coordinates. The setup consists of non-conductive materials and uses profiles for changing the probe's position in x-, y-directions. A threaded fiberglass rod holds the probe and allows for a change of the position in z-direction.

In a first step, the magnetic flux densities in the proximity of the ACT (without the shielding) are measured and compared to the results of the 3-D FEM simulations. The ACT is operated in a series resonant circuit (input configuration ③ from **Fig. 13**), with a primary-side rms current of $I_{meas} = 10\,\mathrm{A}$ at a frequency of 80 kHz. The magnetic fields are measured in the following observation planes:

- xy-planes at $d_{z,\{a,b,c\}} = \{30\,\mathrm{mm}, 200\,\mathrm{mm}, 500\,\mathrm{mm}\}$, cf. **Fig. 18(c)**;
- xz-planes at cuts A, B, and C, cf. **Fig. 18(d)**.

Within cuts A, B, and C, the 11 points marked in **Fig. 18(d)** are selected for the measurements. Except for the points 8 to 11, which are not measured for $d_z = d_{z,c}$ (due to the low fields, there), all points are measured for $d_{z,\{a,b,c\}}$, which yields a total of $33 - 4 = 29$ measurement points.

Figs. 19(a)–(c) present a comparison of simulated (3-D FEM) and measured results, considering an open secondary-side winding. The FEM simulation uses a primary-side rms current of 1 A at a frequency of 80 kHz and thus the measured flux densities, $B_{meas,n}$, are normalized to 1 A,

$$B_{meas,n} = B_{meas} \frac{1\,\mathrm{A}}{I_{meas}}. \tag{2}$$

The average of the absolute value of the relative deviation between the simulated and the measured results is 15.2 % for an open secondary-side winding. As expected, the deviation increases to 26.8 % when considering a short-circuited secondary-side winding (not shown in the figure), which is a consequence of the deviation between the simulated and measured magnetic coupling and hence lower-than-expected secondary-side current for the short-circuit case. However, the open-circuit measurement, which enables a clearly defined current in the primary winding, confirms the high accuracy of the employed 3-D FEM simulation.

[1]The MC162 is a single-axis sensor, has a length of 13 cm, and measures the average of the flux densities along its length. For these reasons, it could not be used for measuring the ACT's stray fields.

Copyright (c) 2021 IEEE. Personal use is permitted. For any other purposes, permission must be obtained from the IEEE by emailing pubs-permissions@ieee.org.

This is the author's version of an article that has been published in this journal. Changes were made to this version by the publisher prior to publication.
The final version of record is available at http://dx.doi.org/10.1109/JESTPE.2021.3060506

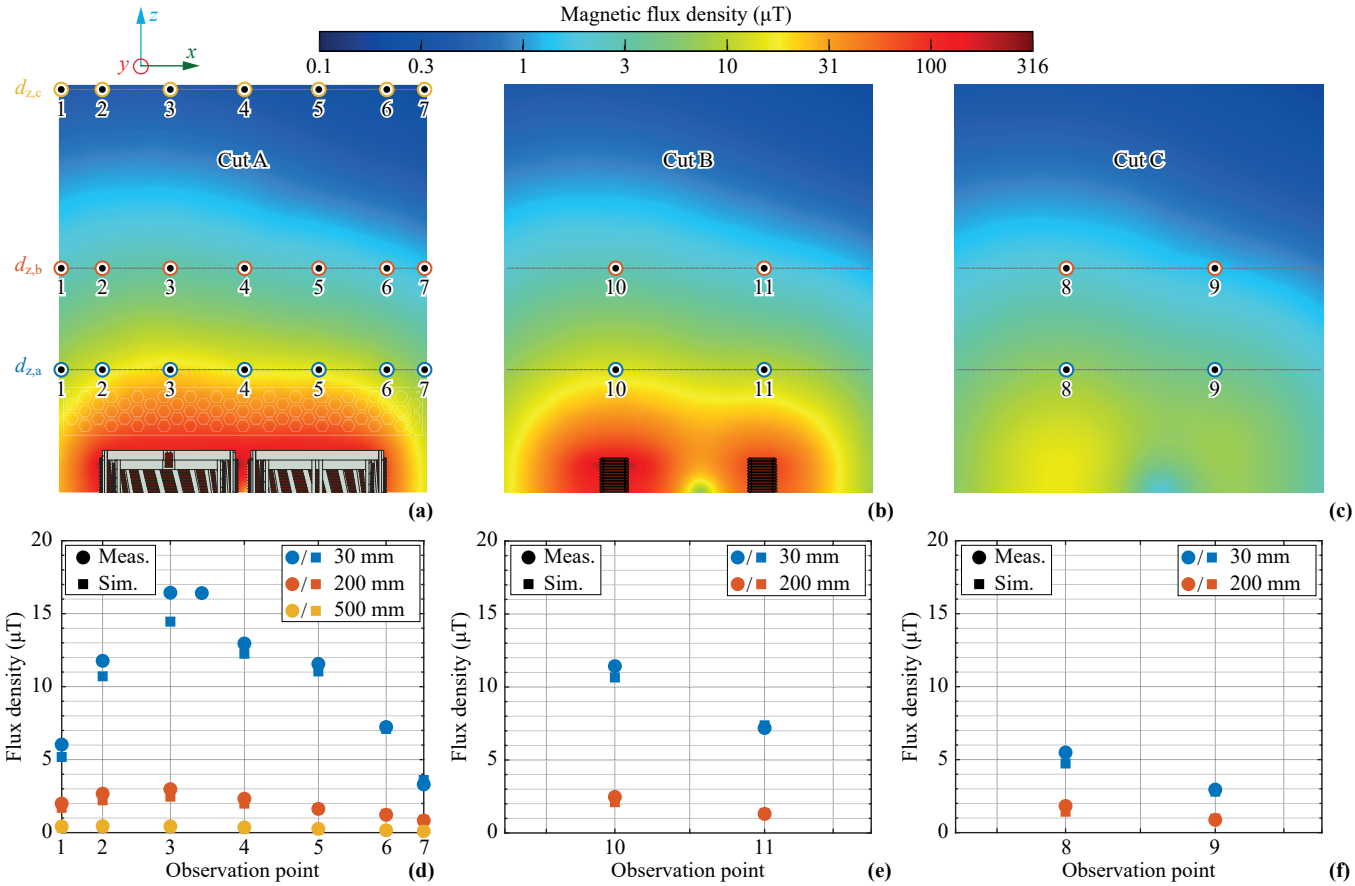

Fig. 19. **(a)–(c)** FEM-simulated flux densities within the cut planes A, B, C defined in **Fig. 18(d)**: ACT without shielding, open-circuit at the secondary-side, primary-side current of 1 A. **(d)–(f)** Measured and simulated rms values of the magnetic flux densities at the observation points defined in **Fig. 18(d)**. The measured results are normalized to a primary-side current of 1 A to allow a comparison with the FEM results.

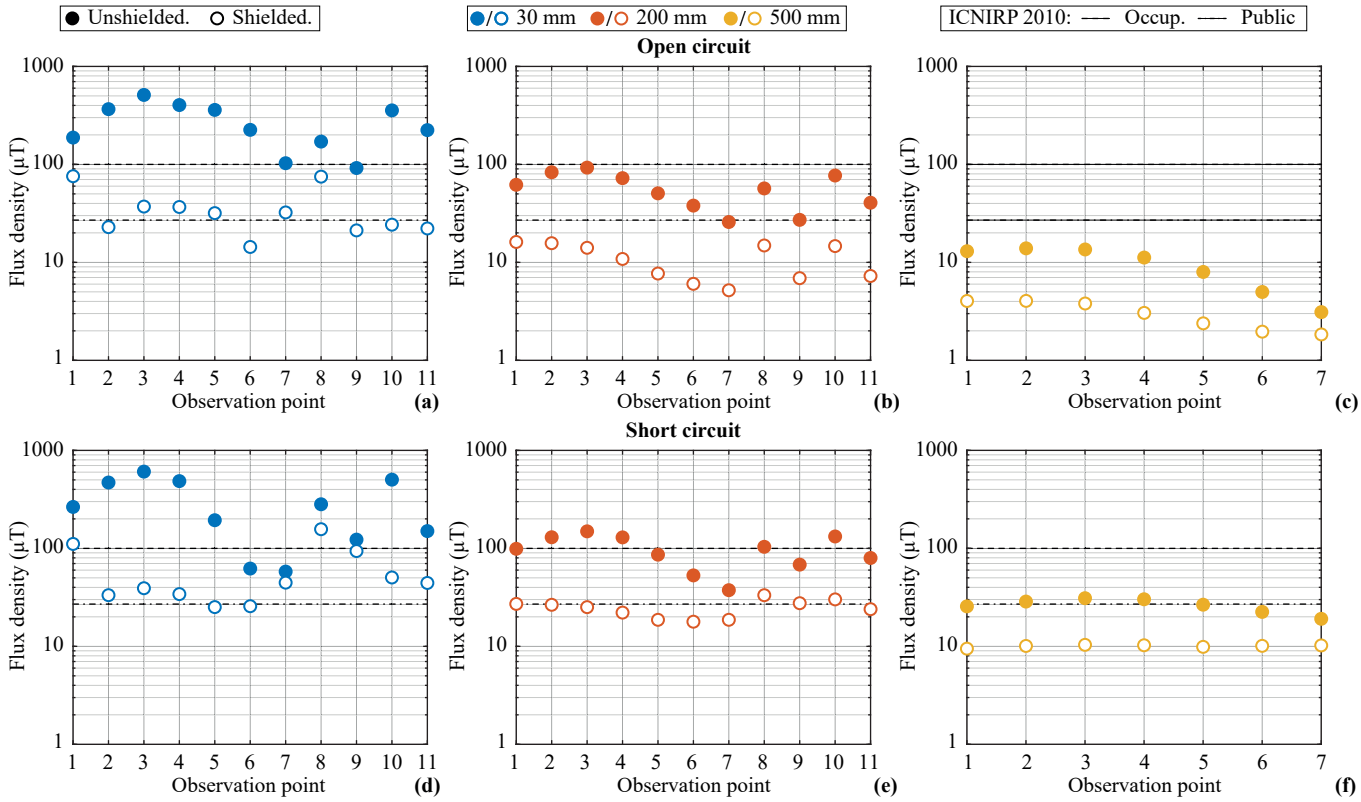

Fig. 20. Measured rms values of the mag. flux densities at the observation points defined in **Fig. 18(d)**, with and without the shielding: **(a)–(c)** secondary-side open-circuit. **(d)–(f)** secondary-side short-circuit. The measured results are scaled to the nominal current, cf. (3). Additionally, the levels for the allowable magnetic field exposure of the general public (27 μT) and of personnel in occupational settings (100 μT) are indicated (ICNIRP 2010, [51]).

Copyright (c) 2021 IEEE. Personal use is permitted. For any other purposes, permission must be obtained from the IEEE by emailing pubs-permissions@ieee.org.

This is the author's version of an article that has been published in this journal. Changes were made to this version by the publisher prior to publication.
The final version of record is available at http://dx.doi.org/10.1109/JESTPE.2021.3060506

3) Shielding efficacy: In a second step, the measurement setup is used to determine the efficacy of the shielding for two different secondary-side configurations, i.e., open- and short-circuit. The open-circuit case is representative for no- or low-load operation, where the ACT's comparably high magnetizing current dominates ($I_\mathrm{m} = 40\,\mathrm{A}$ rms, cf. **Tab. V**, due to the ACT's limited magnetizing inductance). The short-circuit case corresponds to operation at higher, close to rated load where the load current becomes dominant. **Figs. 20(a)–(f)** depict the results that are measured for an rms current of $I_\mathrm{meas} = 10\,\mathrm{A}$ and scaled to the nominal current of $I_\mathrm{p,rms} = 74.6\,\mathrm{A}$ (for $I_\mathrm{s,rms} = 56.6\,\mathrm{A}$) in case of a secondary-side short-circuit and $I_\mathrm{p,rms} = 30.0\,\mathrm{A}$ for open-circuit (considering a first harmonic component of the nominal primary voltage of $V_\mathrm{p,rms} = 4V_\mathrm{1,DC}/(2\sqrt{2}\pi) = 3.2\,\mathrm{kV}$),

$$B_\mathrm{meas,s} = B_\mathrm{meas}\frac{I_\mathrm{p,rms}}{I_\mathrm{meas}}. \tag{3}$$

According to **Figs. 20(a)** and **(d)**, the designed ACT with shielding fulfills ICNIRP 2010 guidelines [51] for occupational exposure at a distance of $30\,\mathrm{mm}$ from the shielding, if the spatial average[2] of the flux density is considered. Furthermore, **Figs. 20(b)** and **(e)** reveal that the ACT with shielding fulfills the guidelines for both occupational and public exposure at a distance of $200\,\mathrm{mm}$ from the shielding when considering the spatial average (even though the local values at points 8 and 10 exceed the reference level for the short-circuit case). Lastly, the measurements in a distance of $500\,\mathrm{mm}$, depicted in **Figs. 20(c), (f)**, show that the guidelines for occupational exposure are met even without the shielding (spatial average). Lastly, as in practice the shielding would be realized as a full enclosure, the flux density in the proximity of the ACT would be even lower (cf. **Fig. 10(c)**), and hence the exposure limits would already be met closer to the shielding. In summary, the shielding provides an adequate efficacy, especially considering that an ACT would typically be located in an area with limited public access, as opposed to IPT systems.

H. Comparison of Optimization and Experimental Results

In addition to the specific validation of individual models discussed throughout the experimental section, e.g., regarding the shielding, the experimental results also enable an overall comparison of the ACT prototype's measured characteristics (e.g., losses, power density) with those obtained from the initial model-based multi-objective optimization described in **Section III-C**.

To do so, we highlight the prototype's location in the performance space shown in **Fig. 7**: the marking ○ corresponds to the built prototype when considering the active part only, i.e., the two sets of coils, corresponding terminal blocks, and isolation barriers. In contrast, the symbol ☆ represents the full ACT prototype, i.e., including the conductive shielding (full enclosure with honeycomb holes), the fans, and mechanical supports etc. The marking ● indicates the performance of the selected design according to the optimization results, as discussed earlier. Furthermore, **Fig. 21** presents mass, volume and loss breakdowns for the three cases.

Regarding the gravimetric power density, **Fig. 21(a)** reveals that the mass of the realized active part matches the optimization results closely ($\gamma = 25.7\,\mathrm{kW/kg}$, including a certain offset to account for fans, isolation etc.). However, the complete prototype's overall gravimetric power density is lower ($\gamma = 16.5\,\mathrm{kW/kg}$), mainly because of the weight of the structural parts required for the mechanical assembly. The mass breakdown reveals the great importance of low-weight realizations of coil formers, supports, fixtures, and insulation components, as they account for more than $55\,\%$ of the prototype's total mass. This relatively high share partly results from prototyping constraints and could be improved with industrial processes. Note that this is usually not the case for conventional MCTs where the weight of the core dominates [46]. Consequently, the gravimetric power density of MCTs is limited to approx. $10\,\mathrm{kW/kg}$ [13].

As shown in **Fig. 21(b)**, the volume of the realized prototype's active part is approximately $50\,\%$ higher compared to the optimization result, which is a consequence of the implemented clearance and creepage distances (see **Section IV**) that demand longer coil formers and isolation barriers. The overall volumetric power density of the complete prototype of $\rho = 2.2\,\mathrm{kW/dm^3}$ is determined by the

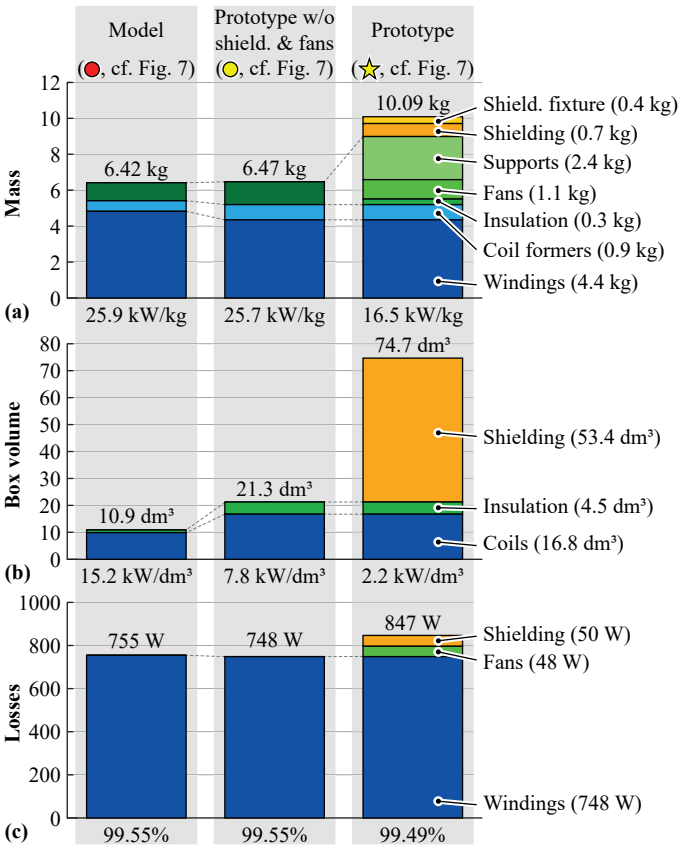

Fig. 21. Comparison of ACT modeling with experimentally validated results (See also **Fig. 7**). Breakdowns of: **(a)** masses; **(b)** box volumes, **(c)** losses. The left column represents results of the model-based optimization; the middle column considers measured results of the prototype's active part only; the right column finally considers the full ACT prototype.

[2]The spatial average is calculated / measured by scanning a planar area equivalent to the area occupied by a standing adult human (projected area). In most instances, a simple vertical, linear scan of the fields over a height of 2 meter is sufficient [52].

Copyright (c) 2021 IEEE. Personal use is permitted. For any other purposes, permission must be obtained from the IEEE by emailing pubs-permissions@ieee.org.

This is the author's version of an article that has been published in this journal. Changes were made to this version by the publisher prior to publication.
The final version of record is available at http://dx.doi.org/10.1109/JESTPE.2021.3060506

box-shaped shielding enclosure, which has been designed a posteriori. Note that smaller enclosures would be possible if higher losses in the shielding would be accepted. It is important to point out that the initial analysis presented in [13] clearly shows that a conventional MCT is the better choice for achieving high compactness, as an up to $50\,\%$ higher volumetric power density can be achieved. However, compactness together with stringent requirements related to insulation and cooling (potting of the windings, handling of increased thermal resistances) render the design of the MCT challenging. In contrast, the clearance (and creepage) distances of the proposed ACT can be easily extended to meet various insulation requirements by changing the NOMEX barrier elements (see **Section IV-A**).

Finally, the loss model used during the optimization (based on 2-D FEM simulations) proves highly accurate (see **Fig. 21(c)**). The loss contributions of the shielding ($6\,\%$ of the total losses) and of the fans ($6\,\%$, whereby one should remember that passive cooling is feasible up to about $70\,\%$ of rated power) reduce the prototype's full-load efficiency ($\eta = 99.49\,\%$) only slightly.

All in all, the relatively straightforward models employed for the Pareto optimization capture the key performance characteristics quite accurately, especially regarding the expected ACT efficiency and the mass of its active part. The now established know-how regarding the mechanical assembly and the dimensions of a suitable conductive shielding could be included in future versions of the optimization procedure. However, as there are various degrees of freedom regarding both, the mechanical assembly and the design of an optimized shielding, which may further depend on specific application scenarios, a decoupled approach as used here might still be attractive to retain full design flexibility.

VI. Transformer Operation in 1:1-DCX

The final section of this paper discusses the overall performance of the ACT-based 1:1-DCX, with a special focus on the ACT's partial-load efficiency.

Since the ACT is a linear system, the previously validated loss models can be evaluated at reduced power levels to calculate the losses of the ACT for partial-load operation. This holds for the losses in the windings and in the conductive shielding (FEM-based calculations). Furthermore, passive cooling is sufficient up to a about $70\,\%$ of the rated power. Hence, the power consumption of the fans must be considered only for higher power levels. **Fig. 22** shows measured (stars) and simulated (circles) distributions of the ACT losses and the corresponding efficiency curve. The partial-load efficiency of the transformer is very high, i.e. $\eta > 99.4\,\%$ applies for a very wide range of the output power, i.e., $P_\mathrm{o} \in [15\%, 100\%] P_\mathrm{N}$. The ACT achieves this high partial-load efficiency despite the high magnetizing current (compared to a conventional MCT) and increased winding losses, which is possible thanks to the absence of core losses. Finally, on the system-level, the relatively high magnetizing current advantageously facilitates ZVS for the 1:1-DCX power semiconductors.

With regard to the overall 1:1-DCX system, the losses of the semiconductors (conduction and switching losses) and the capacitors (resonant and DC-link) as well as the power demand of the fans are considered in a simulation as follows:

- SiC MOSFETs: based on previously published data, e.g., by using experimental data for the switching losses from [43], [53].
- Resonant and DC-link capacitors: modeled based on data sheet information, e.g., the specified dissipation factors are used to determine the losses.
- Converter cooling system: determined based on experimental data from [53].

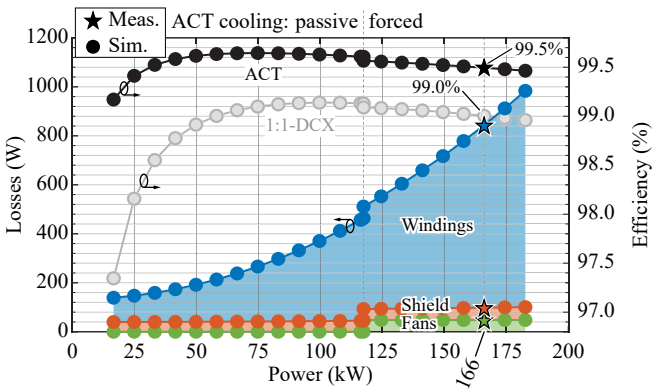

Fig. 22. Measured (★) and simulated (●) distributions of the transformer losses; efficiencies of transformer and 1:1-DCX. At the rated power of $166\,\mathrm{kW}$, the transformer efficiency is $99.5\,\%$, whereas the converter efficiency reaches $99.0\,\%$.

Fig. 22 shows the calculated overall system-level efficiency of the ACT-based 1:1-DCX. At the rated power of $P_\mathrm{N} = 166\,\mathrm{kW}$, the transformer efficiency is $99.5\,\%$, and the converter efficiency reaches $99.0\,\%$, which it even exceeds down to about $35\,\%$ of the rated power.

VII. Conclusion

In this paper the design, realization, and the experimental evaluation of a $166\,\mathrm{kW}$ / $7\,\mathrm{kV}$ air-core transformer (ACT) as part of a DC transformer (DCX), i.e., the DC-DC converter stage of a solid-state transformer (SST) is presented. The realized full-scale prototype of the MV/MF ACT consists of two sets of coaxially arranged solenoids, achieving a relatively high coupling factor of 0.76. Thanks to this construction, a symmetrical design of primary- and secondary-side windings results and partial cancellation of magnetic stray flux is achieved.

The realization of the ACT is of relatively low complexity, as air can be used as an insulation and cooling medium, i.e., the ACT does not require potting material for insulation and thus the corresponding challenges known for conventional magnetic-core transformers (MCTs) are avoided, e.g., dielectric losses, partial discharges, and the need for void-free potting of the windings. Furthermore, the thermal design is simplified as large areas of the transformer coils are available for direct (forced) air cooling. Thus, the ACT can be operated with a winding current density of more than $7\,\mathrm{A/mm^2}$. Also, operation at up to $70\,\%$ of the rated power is feasible with passive cooling (i.e., natural convection) only, e.g., in case of defective fans. These aspects translate into comparably simple and hence cost-effective manufactur-

Copyright (c) 2021 IEEE. Personal use is permitted. For any other purposes, permission must be obtained from the IEEE by emailing pubs-permissions@ieee.org.

This is the author's version of an article that has been published in this journal. Changes were made to this version by the publisher prior to publication.
The final version of record is available at http://dx.doi.org/10.1109/JESTPE.2021.3060506

ing, which is complemented by simplified handling because of the relatively low mass.

The ACT prototype features a nominal insulation voltage of $10\,\mathrm{kV}$. Clearance and creepage distances according to IEC 62477 are realized by adding barrier elements made of NOMEX into the air gaps between primary- and secondary-side windings. In contrast to MCTs, the clearance and creepage distances can be increased by simply extending the length of the barrier elements, i.e., they can be tailored to meet more stringent requirements, e.g., for airborne applications, where longer clearance distances must be used to account for lower air pressure.

To reduce the magnetic stray flux in the proximity of the transformer, a conductive (aluminum) shielding enclosure is designed, built, and tested. With the proposed shielding, the ACT fulfills the ICNIRP 2010 guidelines regarding the magnetic stray flux levels for public exposure at a distance of $200\,\mathrm{mm}$ from the shielding. Adding the shielding enclosure increases the weight by around $10\,\%$, the overall losses by $6\,\%$, and determines the boxed volume of the transformer, yielding a volumetric power density of $2.2\,\mathrm{kW/dm^3}$ (compared to $7.8\,\mathrm{kW/dm^3}$ without the shielding).

The ACT prototype achieves a measured full-load efficiency of $99.5\,\%$ at an operating frequency of $77.4\,\mathrm{kHz}$, and an unprecedented gravimetric power density of $16.5\,\mathrm{kW/kg}$. Moreover, considering the use of $10\,\mathrm{kV}$ SiC MOSFETs, a system-level efficiency of $99\,\%$ is estimated for the complete 1:1-DCX at an output power of $166\,\mathrm{kW}$. In addition, the ACT-based 1:1-DCX is characterized by an extremely flat efficiency curve because of the ACT's low no-load losses. Overall, these properties render the ACT a serious competitor of the MCT. The ACT concept is thus particularly well suited for emerging applications in which robustness, weight, serviceability and cost-effective manufacturing of the transformer are of high importance.

Acknowledgements

The authors are very much indebted to the Swiss Centre for Competence in Energy Research on the Future Swiss Electrical Infrastructure (SCCER-FURIES) for the support of the research in the area of Solid-State Transformer Technology at the ETH Zurich.

References

[1] J. E. Huber and J. W. Kolar, "Applicability of Solid-State Transformers in Today's and Future Distribution Grids," *IEEE Trans. Smart Grid*, vol. 10, no. 1, pp. 317–326, Jan. 2019.

[2] T. Dragicevic, J. C. Vasquez, J. M. Guerrero, and D. Skrlec, "Advanced LVDC Electrical Power Architectures and Microgrids: A Step Toward a New Generation of Power Distribution Networks." *IEEE Electrific. Mag.*, vol. 2, no. 1, pp. 54–65, Mar. 2014.

[3] P. C. Kjaer, Y.-H. Chen, and C. G. Dincan, "DC Collection: Wind Power Plant with Medium Voltage DC Power Collection Network," presented at the ECPE Workshop Smart Transf. Traction Future Grid Appl., Zürich, Switzerland, 2016.

[4] S. Falcones, R. Ayyanar, and X. Mao, "A DC–DC Multiport-Converter-Based Solid-State Transformer Integrating Distributed Generation and Storage," *IEEE Trans. Power Electron.*, vol. 28, no. 5, pp. 2192–2203, May 2013.

[5] B. Hafez, H. S. Krishnamoorthy, P. Enjeti, S. Ahmed *et al.*, "Medium Voltage Power Distribution Architecture with Medium Frequency Isolation Transformer for Data Centers," in *Proc. of the IEEE Appl. Power Electron. Conf. and Expo. (APEC)*, 2014, pp. 3485–3489.

[6] D. Rothmund, T. Guillod, D. Bortis, and J. W. Kolar, "99 % Efficient 10 kV SiC-Based 7 kV/400 V DC-Transformer for Future Data Centers," *IEEE Trans. Emerg. Sel. Topics Power Electron.*, vol. 7, no. 2, pp. 753–767, 2019.

[7] S. Srdic and S. Lukic, "Toward Extreme Fast Charging: Challenges and Opportunities in Directly Connecting to Medium-Voltage Line," *IEEE Electrific. Mag.*, vol. 7, no. 1, pp. 22–31, 2019.

[8] H. Tu, H. Feng, S. Srdic, and S. Lukic, "Extreme Fast Charging of Electric Vehicles: A Technology Overview," *IEEE Trans. Transport. Electrific.*, vol. 5, no. 4, pp. 861–878, Dec. 2019.

[9] S. Castellan, R. Menis, A. Tessarolo, and G. Sulligoi, "Power Electronics for All-Electric Ships with MVDC Power Distribution System: An Overview," in *Proc. of Int. Conf. on Ecological Vehicles and Renewable Energies (EVER)*, 2014, pp. 1–7.

[10] ABB Marine & Ports, "Onboard DC Grid – A System Platform at the Heart of Shipping 4.0," Generations, 2017. [Online]. Available: https://new.abb.com/marine/generations

[11] G. Ulissi, S.-Y. Lee, and D. Dujic, "Solid-State Bus-Tie Switch for Shipboard Power Distribution Networks," *IEEE Trans. Transport. Electrific.*, vol. 6, no. 3, pp. 1253–1264, Sep. 2020.

[12] N. Madavan, "NASA Investments in Electric Propulsion Technologies for Large Commercial Aircraft," in *Proc. of Electric and Hybrid Aerospace Technology Symposium*, 2016.

[13] P. Czyz, T. Guillod, F. Krismer, and J. W. Kolar, "Exploration of the Design and Performance Space of a High Frequency 166 kW/10 kV SiC Solid-State Air-Core Transformer," in *Proc. of the IEEE Int. Power Electron. Conf. (ECCE Asia)*, 2018, pp. 396–403.

[14] M. Armstrong, "Superconducting Turboelectric Distributed Aircraft Propulsion," in *Proc. of Cryogenic Engineering Conf. / Int. Cryogenic Materials Conf.*, 2015.

[15] T. Guillod, R. Faerber, D. Rothmund, F. Krismer *et al.*, "Dielectric Losses in Dry-Type Insulation of Medium-Voltage Power Electronic Converters," *IEEE Trans. Emerg. Sel. Topics Power Electron.*, vol. 8, no. 3, pp. 2716–2732, Sep. 2020.

[16] M. Mogorovic and D. Dujic, "100kW, 10kHz Medium Frequency Transformer Design Optimization and Experimental Verification," *IEEE Trans. Power Electron.*, vol. 34, no. 2, pp. 1696–1708, May 2019.

[17] C. Gammeter, F. Krismer, and J. W. Kolar, "Comprehensive Conceptualization, Design, and Experimental Verification of a Weight-Optimized All-SiC 2 kV/700 V DAB for an Airborne Wind Turbine," *IEEE Trans. Emerg. Sel. Topics Power Electron.*, vol. 4, no. 2, pp. 638–656, Jun. 2016.

[18] R. Bosshard and J. W. Kolar, "Multi-Objective Optimization of 50 kW/85 kHz IPT System for Public Transport," *IEEE Trans. Emerg. Sel. Topics Power Electron.*, vol. 4, no. 4, pp. 1370–1382, Dec. 2016.

[19] R. Bosshard, J. W. Kolar, J. Muehlethaler, I. Stevanovic *et al.*, "Modeling and η - α -Pareto Optimization of Inductive Power Transfer Coils for Electric Vehicles," *IEEE Trans. Emerg. Sel. Topics Power Electron.*, vol. 3, no. 1, pp. 50–64, Mar. 2015.

[20] M. Bojarski, E. Asa, K. Colak, and D. Czarkowski, "A 25 kW Industrial Prototype Wireless Electric Vehicle Charger," in *Proc. of the IEEE Appl. Power Electron. Conf. and Expo. (APEC)*, 2016, pp. 1756–1761.

[21] S. Inoue and H. Akagi, "A Bidirectional Isolated DC–DC Converter as a Core Circuit of the Next-Generation Medium-Voltage Power Conversion System," *IEEE Trans. Power Electron.*, vol. 22, no. 2, Mar. 2007.

[22] T. Guillod, D. Rothmund, and J. W. Kolar, "Active Magnetizing Current Splitting ZVS Modulation of a 7kV/400V DC Transformer," *IEEE Trans. Power Electron.*, vol. 35, no. 2, pp. 1293–1305, 2019.

[23] Q. Zhu, L. Wang, L. Zhang, and A. Q. Huang, "A 10 kV DC Transformer (DCX) Based on Current Fed SRC and 15 kV SiC MOSFETs," in *Proc. of the IEEE Appl. Power Electron. Conf. and Expo. (APEC)*, 2018, pp. 149–155.

[24] L. Wang, Q. Zhu, W. Yu, and A. Q. Huang, "A Medium-Voltage Medium-Frequency Isolated DC–DC Converter Based on 15-kV SiC MOSFETs," *IEEE Trans. Emerg. Sel. Topics Power Electron.*, vol. 5, no. 1, pp. 100–109, Mar. 2017.

[25] G. B. Joung, C. T. Rim, and G. H. Cho, "Modeling of Quantum Series Resonant Converters-Controlled by Integral Cycle Mode," in *Proc. of the IEEE Industry Appl. Society Annual Meeting*, 1988, pp. 821–826.

[26] K. W. Klontz, D. M. Divan, D. W. Novotny, and R. D. Lorenz, "Contactless Power Delivery System for Mining Applications," *IEEE Trans. Ind. Appl.*, vol. 31, no. 1, pp. 27–35, Jan. 1995.

[27] D. A. G. Pedder, A. D. Brown, and J. A. Skinner, "A Contactless Electrical Energy Transmission System," *IEEE Trans. Ind. Electron.*, vol. 46, no. 1, pp. 23–30, Feb. 1999.

[28] M. Trautmann, C. Joffe, F. Pflaum, B. Sanftl *et al.*, "Implementation of Simultaneous Energy and Data Transfer in a Contactless Connector," in *Proc. of the IEEE Wireless Sensors and Sensor Networks Conf. (WiSNet)*, Jan. 2016, pp. 101–104.

[29] C. R. Teeneti, T. T. Truscott, D. N. Beal, and Z. Pantic, "Review of Wireless Charging Systems for Autonomous Underwater Vehicles," *IEEE J. Ocean. Eng.*, early access.

Copyright (c) 2021 IEEE. Personal use is permitted. For any other purposes, permission must be obtained from the IEEE by emailing pubs-permissions@ieee.org.

This is the author's version of an article that has been published in this journal. Changes were made to this version by the publisher prior to publication.
The final version of record is available at http://dx.doi.org/10.1109/JESTPE.2021.3060506

[30] C. Zhao, D. Dujic, A. Mester, J. K. Steinke *et al.*, "Power Electronic Traction Transformer—Medium Voltage Prototype," *IEEE Trans. Ind. Electron.*, vol. 61, no. 7, pp. 3257–3268, Jul. 2014.
[31] A. Foote and O. C. Onar, "A Review of High-Power Wireless Power Transfer," in *Proc. of the IEEE Transport. Electrific. Conf. and Expo. (ITEC)*, Jun. 2017, pp. 234–240.
[32] H. Zhou, J. Chen, Q. Deng, F. Chen *et al.*, "Input-Series Output-Equivalent-Parallel Multi-Inverter System for High-Voltage and High-Power Wireless Power Transfer," *IEEE Trans. Power Electron.*, vol. 36, no. 1, pp. 228–238, Jan. 2021.
[33] R. Bosshard, U. Iruretagoyena, and J. W. Kolar, "Comprehensive Evaluation of Rectangular and Double-D Coil Geometry for 50 kW/85 kHz IPT System," *IEEE Trans. Emerg. Sel. Topics Power Electron.*, vol. 4, no. 4, pp. 1406–1415, Dec. 2016.
[34] J. Deng, W. Li, T. D. Nguyen, S. Li *et al.*, "Compact and Efficient Bipolar Coupler for Wireless Power Chargers: Design and Analysis," *IEEE Trans. Power Electron.*, vol. 30, no. 11, pp. 6130–6140, Nov. 2015.
[35] M. H. Kheraluwala, D. W. Novotny, and D. M. Divan, "Coaxially Wound Transformers for High-Power High-Frequency Applications," *IEEE Trans. Power Electron.*, vol. 7, no. 1, pp. 54–62, Jan. 1992.
[36] L. Heinemann, "An Actively Cooled High Power, High Frequency Transformer with High Insulation Capability," in *Proc. of the IEEE Appl. Power Electron. Conf. and Expo. (APEC)*, vol. 1, 2002, pp. 352–357.
[37] S. S. Baek, S. Bhattacharya, B. Cougo, and G. Ortiz, "Accurate Equivalent Circuit Modeling of a Medium-Voltage and High-Frequency Coaxial Winding DC-link Transformer for Solid State Transformer Applications," in *Proc. of the IEEE Energy Conv. Congress and Expo. (ECCE USA)*, 2012, pp. 1439–1446.
[38] M. S. Rauls, D. W. Novotny, D. M. Divan, R. R. Bacon *et al.*, "Multiturn High-Frequency Coaxial Winding Power Transformers," *IEEE Trans. Ind. Appl.*, vol. 31, no. 1, pp. 112–118, Jan. 1995.
[39] R. Bosshard, *Multi-Objective Optimization of Inductive Power Transfer Systems for EV Charging*. Ph.D. dissertation, ETH Zürich, 2015.
[40] C. Sullivan, "Optimal Choice for Number of Strands in a Litz-Wire Transformer Winding," *IEEE Trans. Power Electron.*, vol. 14, no. 2, pp. 283–291, 1999.
[41] M. Leibl, G. Ortiz, and J. W. Kolar, "Design and Experimental Analysis of a Medium-Frequency Transformer for Solid-State Transformer Applications," *IEEE Trans. Emerg. Sel. Topics Power Electron.*, vol. 5, no. 1, pp. 110–123, 2017.
[42] T. Guillod, J. Huber, F. Krismer, and J. W. Kolar, "Litz Wire Losses: Effects of Twisting Imperfections," in *Proc. of the IEEE Workshop on Control and Modeling for Power Electron. (COMPEL)*, 2017.
[43] D. Rothmund, D. Bortis, and J. W. Kolar, "Accurate Transient Calorimetric Measurement of Soft-Switching Losses of 10-kV SiC mosfets and Diodes," *IEEE Trans. Power Electron.*, vol. 33, no. 6, pp. 5240–5250, Jun. 2018.
[44] *Safety Requirements for Power Electronic Converter Systems and Equipment. Part 1: General*, IEC Std. 62 477-1, 2012.
[45] *Safety Requirements for Power Electronic Converter Systems and Equipment - Part 2: Power Electronic Converters from 1 000 V AC or 1 500 V DC up to 36 kV AC or 54 kV DC*, IEC Std. 62 477-2, 2018.
[46] T. Guillod, *Modeling and Design of Medium-Frequency Transformers for Future Medium-Voltage Power Electronics Interfaces*. Ph.D. dissertation, ETH Zürich, 2018.
[47] vonRoll, "Winding Wires and Litz Wires," 2018. [Online]. Available: https://www.vonroll.com/en/brochure/
[48] *Recommended Practice for Testing Insulation Resistance of Electric Machinery*, IEEE Std. 43-2013, 2014.
[49] Megger, "A Guide To Diagnostic Insulation Testing Above 1 kV," 2018. [Online]. Available: https://megger.com/support/technical-library/
[50] R. Bosshard, J. W. Kolar, and B. Wunsch, "Accurate Finite-Element Modeling and Experimental Verification of Inductive Power Transfer Coil Design," in *Proc. of the IEEE Appl. Power Electron. Conf. and Expo. (APEC)*, 2014, pp. 1648–1653.
[51] *Guidelines for Limiting Exposure to Time-varying Electric and Magnetic Fields (1 Hz to 100 kHz)*, International Commission on Non-Ionizing Radiation Protection Std. ICNIRP, 2010.
[52] *Safety Levels with Respect to Human Exposure to Radio Frequency Electromagnetic Fields, 3 kHz to 300 GHz*, IEEE Std. C95.1, 2005.
[53] D. Rothmund, D. Bortis, J. Huber, D. Biadene *et al.*, "10kV SiC-based Bidirectional Soft-Switching Single-Phase AC/DC Converter Concept for Medium-Voltage Solid-State Transformers," in *Proc. of the IEEE Int. Symposium on Power Electron. for Distrib. Generation Syst. (PEDG)*, 2017.
[54] P. Cairoli, R. Rodrigues, and H. Zheng, "Fault Current Limiting Power Converters for Protection of DC Microgrids," in *Proc. of the IEEE SoutheastCon*, 2017.
[55] P. T. Cheng, S. Y. Yang, Y. Guan, and S. S. Wang, "Design and Implementation of Coaxial Winding Transformers for Isolated DC-DC Converters," in *Proc. of the IEEE Power Conv. Conf. (PCC)*, 2007, pp. 9–15.
[56] K. Satpathi, A. Ukil, and J. Pou, "Short-Circuit Fault Management in DC Electric Ship Propulsion System: Protection Requirements, Review of Existing Technologies and Future Research Trends," *IEEE Trans. Transport. Electrific.*, vol. 4, no. 1, pp. 272–291, 2018.
[57] M. Guacci, D. Bortis, I. F. Kovacevic-Badstübner, U. Grossner *et al.*, "Analysis and Design of a 1200 V All-SiC Planar Interconnection Power Module for Next Generation More Electrical Aircraft Power Electronic Building Blocks," *CPSS Trans. on Power Electron. and Appl.*, vol. 2, no. 4, pp. 320–330, Dec 2017.
[58] *Environmental Conditions and Test Procedures for Airborne Equipment*, Radio Technical Commission for Aeronautics Std. DO-160 G, 2014.

Piotr Czyz (S'14) received his B.Sc. and M.Sc. (summa cum laude) degrees in Electrical Engineering from the Gdansk University of Technology, in 2014 and 2015, respectively. In 2016 he was with C&T Elmech, Poland, working on the development of uninterruptible power supplies. He joined the Power Electronic Systems Laboratory (PES) at ETH Zurich as a visiting researcher in 2017. In August 2017 he began his Ph.D. at PES conducting research in the field of medium-voltage solid-state transformers technologies with the focus on medium-frequency transformers and power semiconductor stages.

Thomas Guillod (M'18) received the M.Sc. degree in electrical engineering and information technology in 2013 from ETH Zurich, Switzerland with a focus on power electronics, numerical analysis, and field theory. In 2013, he joined the Power Electronic Systems Laboratory at ETH Zurich as a Ph.D. student and, in 2018, as a postdoctoral researcher. His current research interests include medium-voltage converters, high-frequency magnetic components, design and optimization methods, and numerical modeling methods.

Florian Krismer (M'12) received the Dipl.-Ing. (M.Sc.) degree in electrical engineering with specialization in automation and control technology from the Vienna University of Technology, Vienna, Austria, in 2004, and the Ph.D. degree in electrical engineering from the Department of Information Technology and Electrical Engineering of ETH Zurich, Zurich, Switzerland, in 2010. He is currently a Research Associate at PES, where he has cosupervised Ph.D. students and has continued with his research in the field of power electronics. He is the author or coauthor of numerous conference and peer-review publications and has received two awards for his publications. His research interests include the analysis, design, and general optimization of power converter systems, e.g., the weight optimization of a bi-directional dc–dc converter for an airborne wind turbine. Furthermore, he conducts research related to the filtering of conducted electromagnetic emissions and collaborated in the littlebox-challenge with respect to the hardware realization.

Copyright (c) 2021 IEEE. Personal use is permitted. For any other purposes, permission must be obtained from the IEEE by emailing pubs-permissions@ieee.org.

This is the author's version of an article that has been published in this journal. Changes were made to this version by the publisher prior to publication.
The final version of record is available at http://dx.doi.org/10.1109/JESTPE.2021.3060506

Jonas Huber (S'11–M'16) received the MSc (with distinction) degree and the PhD degree from the Swiss Federal Institute of Technology (ETH) Zurich, Switzerland, in 2012 and 2016, respectively. Since 2012, he has been with the Power Electronic Systems Laboratory, ETH Zurich and became a Postdoctoral Researcher, focusing his research interests on the field of solid-state transformers, specifically on the analysis, optimization, and design of high-power multi-cell converter systems, reliability considerations, control strategies, and applicability aspects. In 2017, he joined ABB Switzerland Ltd. as an R&D Engineer designing high-power DC-DC converter systems for traction applications. He then returned to the Power Electronic Systems Laboratory as a Senior Researcher in 2020, extending his research scope to all types of WBG-semiconductor-based ultra-compact, ultra-efficient or highly dynamic converter systems.

Johann W. Kolar (M´89–F´10) received his M.Sc. and Ph.D. degree (summa cum laude) from the University of Technology Vienna, Austria, in 1997 and 1999, respectively. Since 1984, he has been working as an independent researcher and international consultant in close collaboration with the University of Technology Vienna. He has proposed numerous novel PWM converter topologies, modulation and control concepts and has supervised 75+ Ph.D. students. He has published 900+ journal and conference papers, and has filed 200+ patents. Dr. Kolar has received 35+ IEEE Transactions and Conference Prize Paper Awards, the 2014 IEEE R. David Middlebrook Achievement Award, and the 2016 IEEE William E. Newell Power Electronics Award. He served from 2001 through 2013 as an associate editor of the IEEE Transactions on Power Electronics. The focus of his current research includes ultra-compact and ultra-efficient SiC and GaN converter systems, advanced variable speed three-phase motor drives, integrated modular motor drives, ultra-high speed motors, and bearingless motors/ actuators. He was elected to the U.S. National Academy of Engineering as an international member in 2021.

Copyright (c) 2021 IEEE. Personal use is permitted. For any other purposes, permission must be obtained from the IEEE by emailing pubs-permissions@ieee.org.